MIT Open Access Articles

MULTIWAVELENGTH OBSERVATIONS OF THE CANDIDATE DISINTEGRATING SUB-MERCURY KIC 12557548B

Massachusetts Institute of Technology

MULTIWAVELENGTH OBSERVATIONS OF THE CANDIDATE DISINTEGRATING SUB-MERCURY KIC 12557548B[*,†,‡]

BRYCE CROLL[1,12], SAUL RAPPAPORT[1], JOHN DEVORE[2], RONALD L. GILLILAND[3], JUSTIN R. CREPP[4], ANDREW W. HOWARD[5],
KIMBERLY M. STAR[3], EUGENE CHIANG[6], ALAN M. LEVINE[1], JON M. JENKINS[7], LOIC ALBERT[8],
ALDO S. BONOMO[9], JONATHAN J. FORTNEY[10], AND HOWARD ISAACSON[11]

[1] Kavli Institute for Astrophysics and Space Research, Massachusetts Institute of Technology, Cambridge, MA 02139, USA; croll@space.mit.edu
[2] Visidyne, Inc., Santa Barbara, CA 93105, USA
[3] Center for Exoplanets and Habitable Worlds, The Pennsylvania State University, 525 Davey Lab, University Park, PA 16802, USA
[4] Department of Physics, University of Notre Dame, 225 Nieuwland Science Hall, Notre Dame, IN 46556, USA
[5] Institute for Astronomy, University of Hawaii at Manoa, 2680 Woodlawn Drive, Honolulu, HI 96822, USA
[6] Departments of Astronomy and of Earth and Planetary Science, University of California at Berkeley,
Hearst Field Annex B-20, Berkeley, CA 94720-3411, USA
[7] SETI Institute/NASA Ames Research Center, M/S 244-30, Moffett Field, CA 94035, USA
[8] Département de physique, Université de Montréal, C.P. 6128 Succ. Centre-Ville, Montréal, QC H3C 3J7, Canada
[9] INAF-Osservatorio Astrofisico di Torino, via Osservatorio 20, I-10025 Pino Torinese, Italy
[10] Department of Astronomy and Astrophysics, University of California, Santa Cruz, CA 95064, USA
[11] Department of Astronomy, University of California, Berkeley, CA 94720, USA

ABSTRACT

We present multiwavelength photometry, high angular resolution imaging, and radial velocities of the unique and confounding disintegrating low-mass planet candidate KIC 12557548b. Our high angular resolution imaging, which includes space-based *Hubble Space Telescope* Wide Field Camera 3 (*HST*/WFC3) observations in the optical ($\sim$0.53 μm and $\sim$0.77 μm), and ground-based Keck/NIRC2 observations in K' band ($\sim$2.12 μm), allow us to rule out background and foreground candidates at angular separations greater than $0\rlap.''2$ that are bright enough to be responsible for the transits we associate with KIC 12557548. Our radial velocity limit from Keck/HIRES allows us to rule out bound, low-mass stellar companions ($\sim$0.2 $M_\odot$) to KIC 12557548 on orbits less than 10 yr, as well as placing an upper limit on the mass of the candidate planet of 1.2 Jupiter masses; therefore, the combination of our radial velocities, high angular resolution imaging, and photometry are able to rule out most false positive interpretations of the transits. Our precise multiwavelength photometry includes two simultaneous detections of the transit of KIC 12557548b using Canada–France–Hawaii Telescope/Wide-field InfraRed Camera (CFHT/WIRCam) at 2.15 μm and the *Kepler* space telescope at 0.6 μm, as well as simultaneous null-detections of the transit by *Kepler* and *HST*/WFC3 at 1.4 μm. Our simultaneous *HST*/WFC3 and *Kepler* null-detections provide no evidence for radically different transit depths at these wavelengths. Our simultaneous CFHT/WIRCam detections in the near-infrared and with *Kepler* in the optical reveal very similar transit depths (the average ratio of the transit depths at $\sim$2.15 μm compared with $\sim$0.6 μm is: 1.02 $\pm$ 0.20). This suggests that if the transits we observe are due to scattering from single-size particles streaming from the planet in a comet-like tail, then the particles must be $\sim$0.5 μm in radius or larger, which would favor that KIC 12557548b is a sub-Mercury rather than super-Mercury mass planet.

Key words: eclipses – infrared: planetary systems – planetary systems – stars: individual (KIC 12557548) – techniques: photometric

Online-only material: color figures

1. INTRODUCTION

Rappaport et al. (2012) presented intriguing, perplexing, and downright peculiar *Kepler* observations of the K-dwarf star,

---

KIC 12557548. The *Kepler* space telescope's (Borucki et al. 2009) observations of this star displayed repeating dips every $\sim$15.7 hr, which varied in depth from a maximum of $\sim$1.3% of the stellar flux to a minimum of $\sim$0.2% or less without a discernible rhyme or reason to explain the depth variations. In addition, the occultations were not the iconic transit-like shape we have come to expect from extrasolar planets or binary stars but exhibited an obvious ingress/egress asymmetry, with a sharp ingress followed by a longer, more gradual egress. A non-detection of ellipsoidal light variations allowed an upper limit on the mass of the occulting object to be set at three Jupiter masses, and thus prompted the question of what was causing this odd photometry? The answer the authors proposed was that the peculiar *Kepler* observations of KIC 12557548 (hereafter KIC 1255) are due to a gradually disintegrating low-mass (super-Mercury) planet, KIC 12557548b (hereafter KIC 1255b). The thought process is that this putative planet, with its extremely

short orbital period, is being roasted by its host star and is throwing off material in fits and starts; at each passage in front of its parent star, the different amount of material being discarded by the planet leads to differences in the resulting optical depth, thus explaining the obvious transit depth variations. The clear ingress/egress asymmetry of the transit is then due to the fact that the material is streaming behind the planet, forming a long comet-like tail that obscures the star for a larger fraction of the orbit.

Naturally, observations as odd as those presented by Rappaport et al. (2012), and an explanation as exotic as a disintegrating super-Mercury, invited a great deal of skepticism from the astronomical community. Alternative theories that have been discussed to explain the observed photometry include: (1) a bizarre *Kepler* photometric artifact; (2) a background blended eclipsing binary[13]; (3) an exotically chaotic triple; or (4) a binary that is orbiting KIC 12557548 wherein one member of the binary system is a white dwarf fed by an accretion disk (Rappaport et al. 2012).

Inspired by the Rappaport et al. (2012) result, there have been a number of modeling efforts to interpret the bizarre *Kepler* observations that seem to reinforce the possibility that the photometry of KIC 1255 is caused by scattering off material streaming from a disintegrating low-mass planet. Dust scattering models confirm the viability of the disintegrating planet scenario featuring a comet-like tail trailing the planet, composed of submicron-sized grains (Brogi et al. 2012), or up to 1 μm (0.1–1.0 μm) sized grains (Budaj 2013). These efforts suggest that the minute brightening just prior to transit can be readily explained by enhanced forward scattering from this dust cloud, while the ingress/egress asymmetry can be explained by a comet-like dust tail that has a particle density or size distribution that decreases with distance from the planet. The richness of the *Kepler* data on KIC 1255b has led to suggestions of evolution of the cometary tail (Budaj 2013) and that the comet is best explained by a two component model, with a dense coma and inner tail and a diffuse outer tail (Budaj 2013; van Werkhoven et al. 2014). Another effort by Kawahara et al. (2013) suggests that the observed transit depth variability may correlate with the stellar rotation period, and thus the presumed variable mass loss rate of the planet may be a byproduct of the stellar activity, specifically ultraviolet and X-ray radiation. Perez-Becker & Chiang (2013) argue, from the results of a hydrodynamical wind model, that we may be observing the final death throes of a planet catastrophically evaporating and that KIC 1255b may range in mass from 0.02–0.07 $M_\oplus$ (less than twice that of the Moon to greater than Mercury), although for most solutions, the mass of KIC 1255b is less than that of Mercury. We note that subsequent to the submission of this work, there has been an announcement of a second low-mass planet candidate, possibly hosting a comet-like tail (Rappaport et al. 2014).

One proposed method for elucidating the unknown nature of the material that is supposedly occulting KIC 1255, is multi-wavelength simultaneous observations of the transit of the object. As the efficiency of scattering diminishes for wavelengths longer than the approximate particle size (Hansen & Travis 1974), and given the inference of submicron-sized grains in the dust tail of this object (Brogi et al. 2012; Budaj 2013), one might expect that infrared and near-infrared photometry of the transit of KIC 1255b would display significantly smaller depths than those displayed in the optical. Determining that the transit depth of KIC 1255b is wavelength dependent, with smaller depths in the near-infrared than the optical, would therefore strongly favor the explanation of scattering from a dust tail with submicron-sized particles.

Here, we present an assortment of different observations of KIC 1255 that were obtained in order to either bolster or rule out the disintegrating low-mass planet scenario. In addition to the *Kepler* photometry that we analyze here, these various observational data include: (1) two Canada–France–Hawaii Telescope/Wide-field InfraRed Camera (CFHT/WIRCam) Ks-band ($\sim$2.15 μm) photometric detections of the KIC 1255b transit with simultaneous *Kepler* photometric detections, (2) simultaneous photometric non-detections of the KIC 1255b transit with the *Hubble Space Telescope* Wide Field Camera 3 (*HST*/WFC3) F140W and *Kepler* photometry, (3) *HST*/WFC3 high angular resolution imaging of KIC 1255 in the F555W ($\lambda \sim 0.531$ μm) and F775W ($\lambda \sim 0.765$ μm) bands, (4) Keck/NIRC2 ground-based adaptive optics (AO) (tip/tilt only) high angular resolution imaging of KIC 1255 in the K' band ($\lambda \sim 2.124$ μm), and (5) Keck/HIRES radial velocity (RV) observations of KIC 1255. The high angular resolution imaging observations allow us to rule out nearby background/foreground companions as close as 0.″2 to KIC 1255. Our KECK/HIRES RV observations allow us to rule out low-mass stellar companions ($\sim$0.2 $M_\odot$) for orbital periods $\lesssim$10 yr. This significantly reduces the parameter space for nearby companions to KIC 1255, and therefore reduces the odds that the unique *Kepler* photometry that Rappaport et al. (2012) reported is due to a binary or higher-order multiple masquerading as a planetary false positive. Our simultaneous *Kepler* and near-infrared detections of the transit of KIC 1255b appear to report similar depths; as a result, if the source of the photometry we observe is a dust tail trailing a disintegrating planet composed of single-sized particles, then the particles are at least $\sim$0.5 μm in radius. Particles this large can likely only be lofted from a low-mass planet, suggesting that KIC 1255b might best be described as a sub-Mercury mass planet.

2. OBSERVATIONS AND ANALYSIS

2.1. Kepler Photometry

We start by presenting an analysis of the *Kepler* data of KIC 1255. We analyze all if the long cadence (quarters 1–16 at the time of writing; 29.4 minute sampling) and short cadence (quarters 13–16; 58.8 s sampling) pre-search data conditioning simple aperture photometry (PDCSAP) of this star. KIC 1255 displays obvious rotational modulation with a period of $\sim$22.9 days, which varies between 1% and 4% of the observed stellar flux; we remove this modulation by employing a cubic spline. To ensure that KIC 1255b's variable and asymmetric transit depth in no way impact our starspot removal technique, we cut out all data in the transit before calculating our cubic spline; that is, we phase the data to the orbital period of the putative planet (where phase, $\phi = 0.5$ denotes the midpoint of the transit), cut out all data between phases $\phi = 0.4$–0.7,[14] and then bin the data every $\sim$10 hr. After calculating the cubic spline on the binned *Kepler* data with the transits removed, we apply the cubic spline to all of the unbinned *Kepler* data and apply a 10σ cut to remove outliers; we thus produce a light curve

---

[13] Although how this would explain the ingress/egress asymmetry, or the transit depth variations remains a mystery.

[14] The asymmetric cut around the midpoint of the transit is obviously due to the asymmetric shape of the transit.

Table 1
CFHT, *HST*, and *Kepler* Photometry of KIC 1255

Parameter	CFHT Transit 1	*Kepler* Transit 1	CFHT Transit 2	*Kepler* Transit 2	*HST* Transit	*Kepler* Transit 3
A	$1.107^{+0.293}_{-0.276}$	$1.036^{+0.103}_{-0.111}$	$1.214^{+0.193}_{-0.241}$	$1.268^{+0.103}_{-0.103}$	$0.058^{+0.051}_{-0.066}$	$0.149^{+0.090}_{-0.102}$
A_{Corr}	1.09 ± 0.32	n/a	1.23 ± 0.27	n/a	n/a	n/a
t_{transit} (BJD-2456150)	$3.881^{+0.004}_{-0.005}$	$3.877^{+0.002}_{-0.003}$	$22.841^{+0.004}_{-0.005}$	$22.830^{+0.001}_{-0.001}$	180.337^{a}	180.337^{a}
y_o	$0.00100^{+0.00053}_{-0.00059}$	$-0.00030^{+0.00014}_{-0.00014}$	$0.00056^{+0.00046}_{-0.00042}$	$0.00027^{+0.00015}_{-0.00014}$	$0.00007^{+0.00022}_{-0.00024}$	$0.00146^{+0.00016}_{-0.00016}$
3σ upper limit on A	1.865	1.368	1.936	1.585	0.354	0.474

Notes. [a] We fix t_{transit} to the predicted midpoint of the transit for this analysis due to the fact we are unable to detect the transit on this occasion.
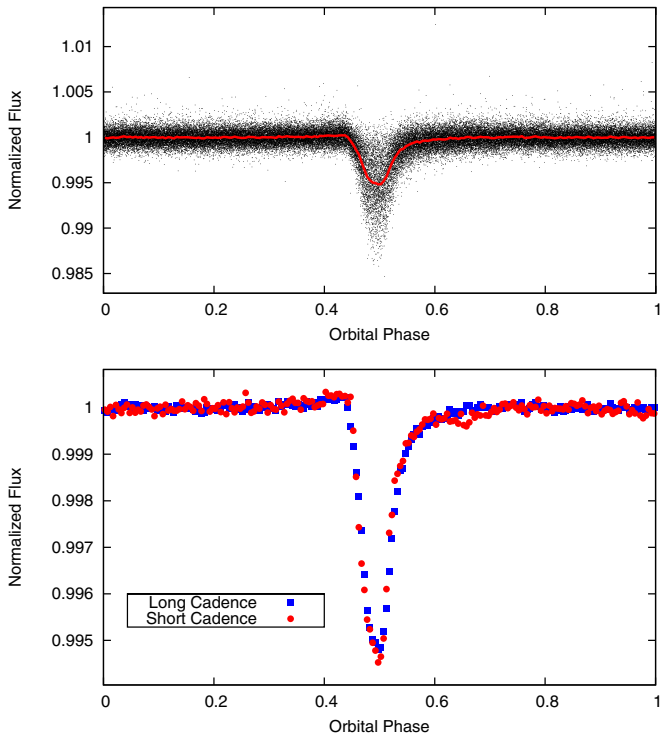

Figure 1. Top panel: *Kepler* long cadence photometry (black points) of KIC 1255 phased to the orbital period of the candidate planet (~15.685 hr). The red line is the binned mean of the orbital phase-folded light curve. Bottom panel: the binned mean of the phase-folded light curve (every $\phi = 0.005$ in phase) of the short cadence (red circles) and long cadence (blue squares) photometry.
(A color version of this figure is available in the online journal.)

of KIC 1255 with the obvious rotational modulation removed. The spot-corrected, phase-folded, long cadence light curve of KIC 1255 is presented in the top panel of Figure 1; the short cadence data are similar but have much higher scatter per point. We present the phase-folded, binned mean of the long and short cadence data in the bottom panel of Figure 1. We note that the short cadence data display a marginally narrower transit and appears to have an extra, brief, enhanced decrement in flux following the transit (i.e., near phase $\phi = 0.65$) that is not visible in the long cadence photometry.

To compare the *Kepler* photometry to our CFHT ground-based (Section 2.2) and *HST* space-based (Section 2.3.1) photometry, we also present the *Kepler* PDCSAP photometry, without the spline correction. Given the asymmetric transit profile and varying transit depth displayed in the *Kepler* photometry, we choose to fit our individual *Kepler* transits (and the simultaneous CFHT and *HST* photometry) by scaling the mean transit profile of the short cadence *Kepler* photometry by a multiplica-

tive factor, A. Therefore, the function we use to fit our data, $g(t)$, is compared to the mean of the phase-folded short cadence photometry, $f(t)$ (shown in the bottom panel of Figure 1), by

$$g(t) = 1 + A\,[f(t - t_{\mathrm{transit}}) - 1] + y_o, \qquad (1)$$

where y_o is simply a vertical offset, and t_{transit} is the mid-transit time (defined as the minimum of the phase-folded mean of the short cadence photometry, at phase $\phi = 0.5$). We note that a value of $A = 1$ corresponds to a KIC 1255b transit depth of 0.55% of the stellar flux, as shown in the bottom panel of Figure 1. We note that, by multiplying our phase-folded mean by A, we are scaling up or down the size of the apparent forward-scattering peak, as well as the depth of the transit.[15] To fit our *Kepler* transits, as well as the CFHT and *HST* transits that follow,[16] we employ Markov Chain Monte Carlo (MCMC) techniques (as described for our purposes in Croll 2006). In Figures 2 and 3, we present the PDCSAP short-cadence *Kepler* photometry of KIC 1255b which was obtained simultaneously with the CFHT and *HST* photometry, as well as the best-fit scaled profile, $g(t)$, of the mean short-cadence *Kepler* profile, $f(t)$. We assume an error on the *Kepler* data for our MCMC fitting based on the rms of the residuals to the best-fit model. The associated best-fit parameters are presented in Table 1.

2.2. CFHT/WIRCam Photometry

We obtained two Ks band (~2.15 μm) WIRCam (Puget et al. 2004) photometric data sets of the transit of KIC 1255 ($K \sim 13.3$). Data sets were obtained on the evenings of 2012 August 13 and 2012 September 1 (Hawaiian Standard Time). The observations lasted for ~6.5 hr and ~5 hr, respectively. High wind impacted the image quality for the first set of observations (2012 August 13); the second set of observations were of photometric quality throughout the night (2012 September 1). Reduction of the data and aperture photometry was performed as detailed in Croll et al. (2010a, 2010b). Although WIRCam offers a $21' \times 21'$ field of view, we only utilize reference stars from the same detector as our target, therefore resulting in a $10' \times 10'$ field of view. We employ a range of aperture radii for our CFHT photometry (as discussed below in Section 2.2.1), and subtracted the sky in all cases using an annulus with an inner and outer radius of 14 and 20 pixels, respectively. To determine the fractional contribution of the square pixels

---

[15] This assumption is likely reasonable, as the analysis of Brogi et al. (2012) indicates that the deeper transits appear to display a larger forward-scattering peak just prior to transit, as one might naively expect if the deeper transit is being caused by a larger amount of material occulting the star.

[16] We note that we do not account for the effect of the various exposure times of our CFHT, *HST*, and *Kepler* data on estimating the parameters of interest in Equation (1), as such differences are negligible given our short exposure times (~5 s to ~1 minute; please see Kipping 2010).
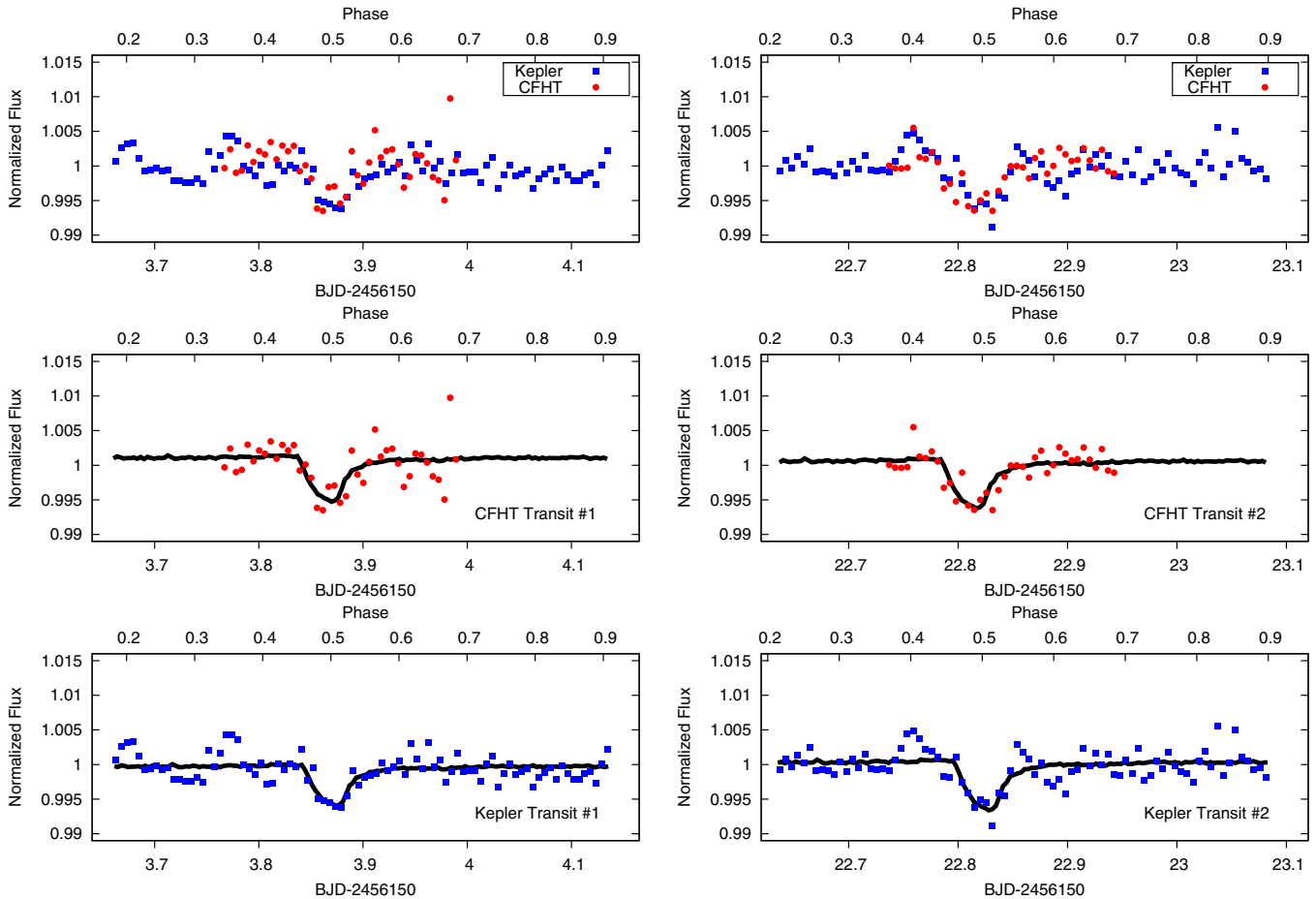
Figure 2. CFHT/WIRCam Ks-band photometry (red circles) and *Kepler* photometry (blue squares) of the transit of KIC 1255b obtained on the nights of 2012 August 13 (left panels) and 2012 September 1 (right panels; Hawaiian Standard Time). Both sets of data are binned every eight minutes. The black lines in the bottom two sets of panels indicate the best-fit transit model for each set of data; the transit model is a scaled version of the mean of the short cadence, phase-folded *Kepler* light curve ($g(t)$; see Section 2.1).

(A color version of this figure is available in the online journal.)

at the edge of the circular aperture, we multiply the flux of these pixels by the fraction of the pixels that falls within our circular aperture; we determine this fractional contribution using the GSFC Astronomy Library IDL procedure *pixwt.pro*. The exposure times were 25 s, with an overhead for read out and saving exposures of 7.38 s, resulting in an overall duty-cycle of ∼76%. The telescope was defocused to 0.9 mm for both observations. In both cases, at the conclusion of the observations, the airmass increased to beyond 2.0; we noticed reduced precision in the resulting light curves once the airmass rose above a value of 1.6. As a result, we exclude all data with an airmass greater than this latter value in the following analysis. Our CFHT photometry is presented in the middle panel of Figure 2, using aperture radii of 7 and 9 pixels for our first and second CFHT transits, respectively. After the subtraction of our best-fit models, we achieve an rms precision of 7.1×10^{-3} and 6.5×10^{-3} per exposure for our first and second transit, respectively. This compares to the expected photon noise limit of 1.15×10^{-3} per exposure, or 3.52×10^{-3} once other noise sources (read noise, dark, and sky noise, where the sky is the dominant component) are taken into account. We compare our photometric precision to the Gaussian noise expectation of one over the square-root of the bin size in Figure 4. Both data sets scale down above this limit, indicative of correlated noise; some of this correlated noise is likely astrophysical as the *Kepler*

data display obvious modulation, likely due to granulation or evolution of starspots, plages, etc., that appears to be partially replicated in the CFHT near-infrared photometry.

We fit our CFHT transits with the scaled version of the short cadence, phase-folded *Kepler* light curve ($g(t)$; Section 2.1). The best-fit transits are displayed in Figure 2, and the associated transit depths, A, compared to the mean *Kepler* transit depth, are given in Table 1.

We also note that, as our CFHT photometry has slightly superior angular resolution than the coarse *Kepler* pixels, our CFHT photometry allows us to place a limit on the angular separation of the transiting object from KIC 1255. Assuming the transits we observe in our CFHT photometry are due to the same object causing the transits we observe in the *Kepler* data, and given the 7–9 pixel aperture we use here and WIRCam's 0″.3 pixel scale, the object causing the transits we associate with the candidate planet KIC 1255b cannot be due to a companion more than ∼2″ away from KIC 1255.

2.2.1. Correlations with Aperture Size and Number of Reference Stars

We also search for correlations in our CFHT photometry between the measured transit depth, our choice of aperture size, and the choice of the number of reference stars. With our other CFHT photometry of hot Jupiters (B. Croll et al., in
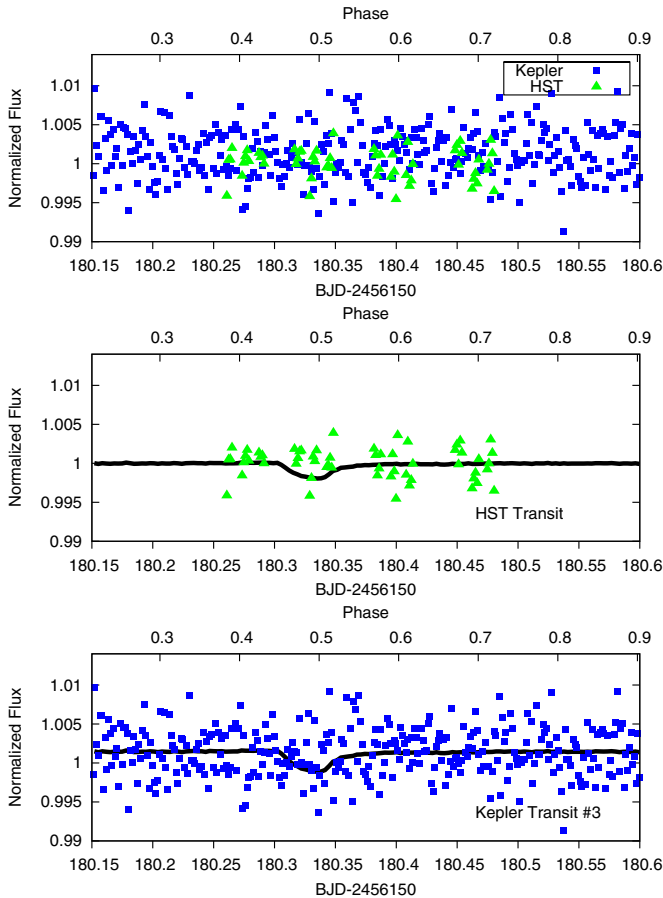
Figure 3. *HST* F140W filter photometry (1.4 μm; green triangles) and *Kepler* photometry (blue squares) of the transit of KIC 1255b obtained on 2013 February 6 (UTC). The *Kepler* and *HST* data are binned every two minutes. The black lines in the bottom two panels indicate the 3σ upper limit on the transit depth obtained by scaling the mean of the short cadence, phase-folded *Kepler* light curve ($g(t)$; see Section 2.1).

(A color version of this figure is available in the online journal.)

preparation), in some cases, we noticed moderate correlations between the secondary eclipse or primary transit depths and the aperture radius chosen for aperture photometry, or the choice of the ensemble of reference stars we use to correct our photometry. Despite these changes in the transit/eclipse depth, the differences in the rms of the residuals to the best-fit model were often negligible. Therefore, we were confronted with a range of seemingly equal good fits to the data, where, troublingly, the parameter of interest, the transit/eclipse depth, varied significantly. As a result, rather than quoting just the best fit of a single aperture and reference star combination, we quote the weighted mean of a number of aperture photometry and reference star combinations and scale up the associated error to take these correlations into account.

To determine the best reference star and aperture radius combination, we generally use the rms of the residuals multiplied by β, which parameterizes the amount of time-correlated red noise in the photometry. β is defined, employing the methods of Winn et al. (2008), as the factor by which the residuals scale above the Gaussian noise expectation (see Figure 4); to determine this number, we take the average of bin sizes between 10 and 80 binned points. In general, we have noticed that the rms $\times \beta$ of the residuals is a superior metric to determine the best aperture size/reference star combination than simply the rms; for our near-infrared photometry, which gener-

ally suffers from high sky background compared to the optical, the rms of the residuals generally reaches a minimum for relatively small apertures, as one is able to reduce the impact of the high sky background. However, these small apertures often suffer from time-correlated red noise (high βs), as during moments of poor seeing or tracking errors, a small fraction of the light falls outside these small apertures. A small complication for our CFHT/WIRCam Ks-band photometry of KIC 1255, however, is that, as noted above, we believe that some of the correlated red noise we observe is genuine, as it reproduces, in part, the short-term variations visible in the *Kepler* optical photometry. Therefore, we qualitatively noticed that the most useful metrics were the rms of the residuals for the first CFHT/WIRCam transit and the rms of the residuals multiplied by β for the second CFHT/WIRCam transit; this combination produced the most satisfactory results. For this reason, we used these two different metrics to determine the best reference star ensemble and aperture size combination below.

In Figure 5, we present the correlations with aperture radius and the number of stars in our reference star ensemble for both our first and second CFHT transit of KIC 1255b. For both cases, we display the variation in rms, and the variation in rms multiplied by β, for a variety of aperture radii and different number of reference stars in the ensemble, as well as the associated variation in the associated KIC 1255b transit depths, as parameterized by A. In the top set of panels, we display the rms, rms $\times \beta$, and A values for a variety of aperture sizes for the best seven-star reference ensemble.[17] In the bottom set of panels, we display the rms, rms $\times \beta$, and A values for ensembles of different numbers of reference stars, for a 7.0 pixel aperture (first CFHT transit) and a 9.0 pixel aperture (second CFHT transit).

We note that the differences in the parameter of interest, A, are modest for most combinations of reference star ensembles and aperture radii. Nevertheless, it is important to scale up our errors on A to take these correlations into account. To determine the transit depth of KIC 1255b once correlations with reference star ensemble and aperture radius are taken into account, A_{Corr}, we take the weighted mean of all values with an rms no greater than 10% above the minimum rms for our first transit,[18] and for our second CFHT transit, we take all values with an rms $\times \beta$ no greater than 40%[19] and 10% above the minimum rms $\times \beta$ value (these are denoted by the dotted horizontal line in Figure 5) for the various aperture radii, and number of reference stars, respectively.[20] To determine the error on A_{Corr}, we calculate the mean error of all of the values used to determine A_{Corr} and add to this value, in quadrature, the standard deviation of the A values. The A_{Corr} values for the first and second CFHT transit are given in Table 1. The error on A_{Corr} for both transits has increased marginally compared with that on A before the

---

[17] We use a seven-star reference ensemble, as this gave the minimum rms of the residuals for the first transit and the minimum rms $\times \beta$ of the residuals for the second transit.
[18] We therefore average aperture radii of 7.0–9.5 pixels and 4–11 reference stars for our first CFHT transit.
[19] We use 40%, rather than the 10% utilized for the other reference star/aperture size combinations due to the fact that the aperture radii 5.5 and 6.0 display such small rms $\times \beta$ (the top right panel of Figure 5). This is due to the fact that, for these aperture radii, a different seven-star reference ensemble was chosen automatically by the routine to have the smallest rms. This reference star ensemble features stars that are not as bright and display considerably worse rms $\times \beta$ values for larger aperture sizes. We prefer the 9.0 pixel reference star ensemble and present it in Figure 2.
[20] We therefore average aperture radii of 5.5, 6.0, and 7.5–12.5 pixels, and 4–11 reference stars.
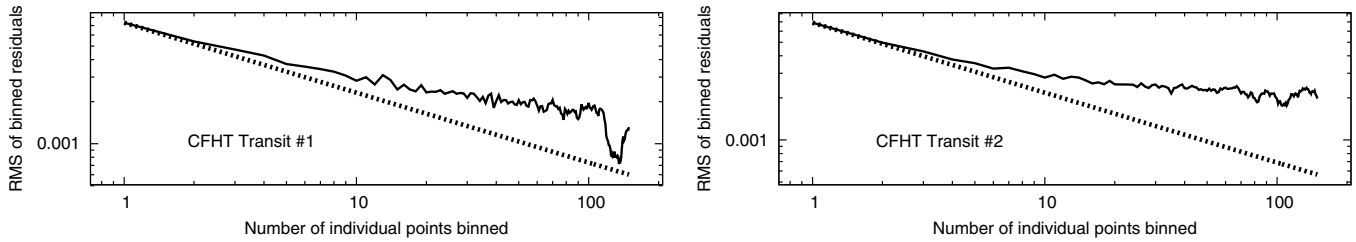
Figure 4. rms of our photometry after the subtraction of our best fit (solid line) for our CFHT/WIRCam Ks-band photometry of our first transit (left) and our second transit (right). The dashed line in each panel displays the one over the square-root of the bin-size expectation for Gaussian noise.
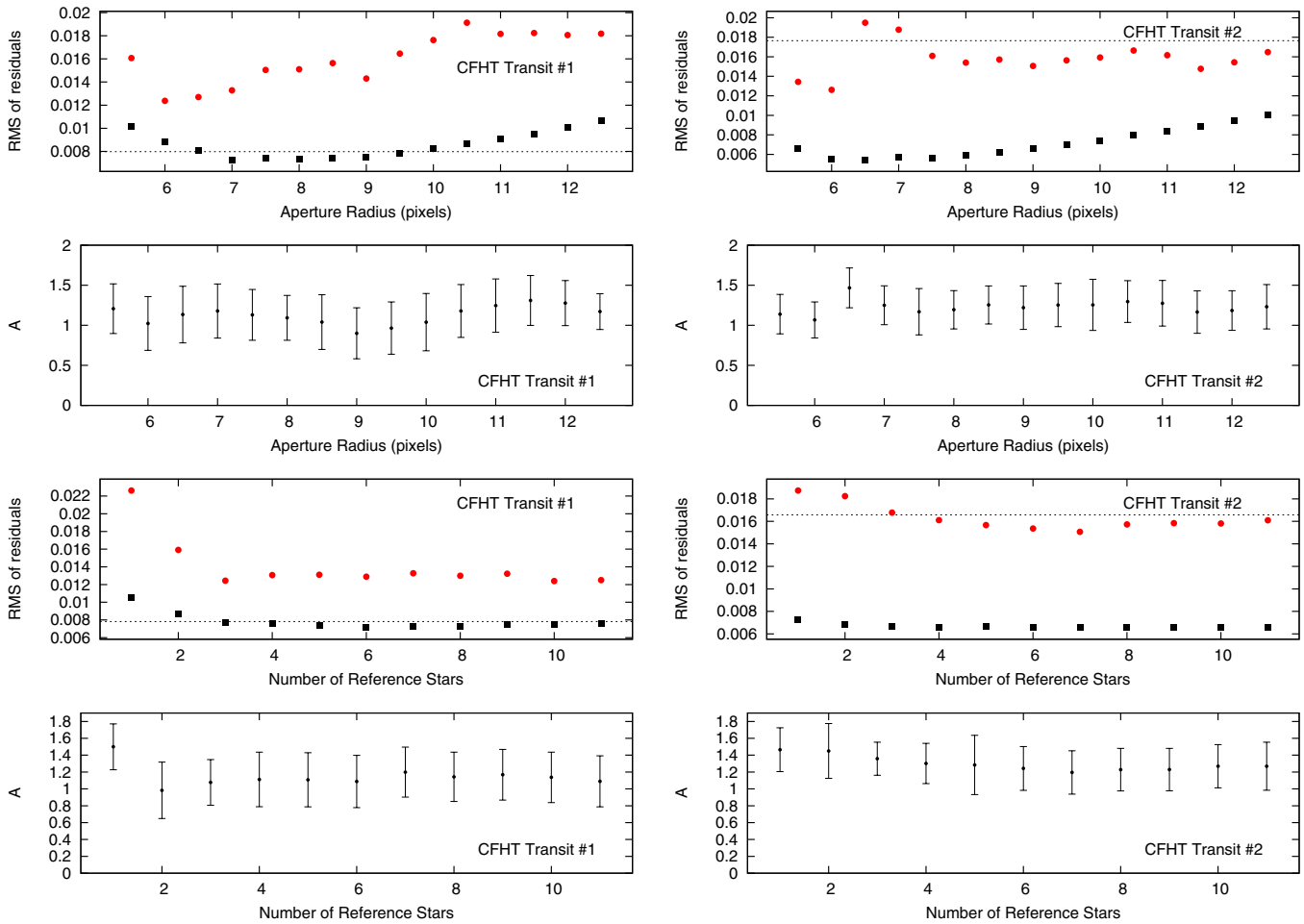

Figure 5. Top panels: the rms of the residuals from the best-fit MCMC fit (black squares), and the residuals multiplied by the relevant β factor (red circles) for each of the various aperture sizes (using the best seven reference stars), for our first (left) and second (right) transit CFHT/WIRCam Ks-band transit. Second from top set of panels: the associated measured MCMC transit depths, A. The bottom four panels are the same as the top four, except they display the rms and A values for the different number of reference stars for our first transit (left; 7.0 pixel aperture radius) and our second transit (right; 9.0 pixel aperture radius). We average over all A values for aperture radii and number of reference stars with rms values (black points) below the black dotted line for the first CFHT transit (left panel); for the second transit (right panel), we average all A values with rms×β values (red points) below the black dotted line.

(A color version of this figure is available in the online journal.)

correlations with the number of stars in the reference ensemble and the aperture size were taken into account.

2.3. HST Photometry and Imaging

On 2013 February 6 (UTC), we observed a transit of KIC 1255 with the *HST* WFC3 (Dressel et al. 2010) over five orbits (*HST* Proposal GO-12987, P.I.: S. Rappaport). The first orbit was devoted to high angular resolution imaging observations of KIC 1255 in order to rule out nearby background and foreground objects or companions to this object; these observations are detailed in Section 2.3.2. The second through fifth *HST* orbits

were devoted to F140W ($\lambda \sim 1.39$ μm) photometry of the transit of KIC 1255; these observations are detailed below in Section 2.3.1.

We use the calibrated, flat-fielded *flt* files from WFC3's calwf3 reduction pipeline.

2.3.1. HST Photometry

We obtained *HST*/WFC3 photometry over four *HST* orbits of the transit of KIC 1255 in the F140W filter ($\lambda \sim 1.39$ μm) on 2013 February 6 (UTC). The exposure times were 4.27 s; observations were obtained every 22.98 s, resulting in a duty
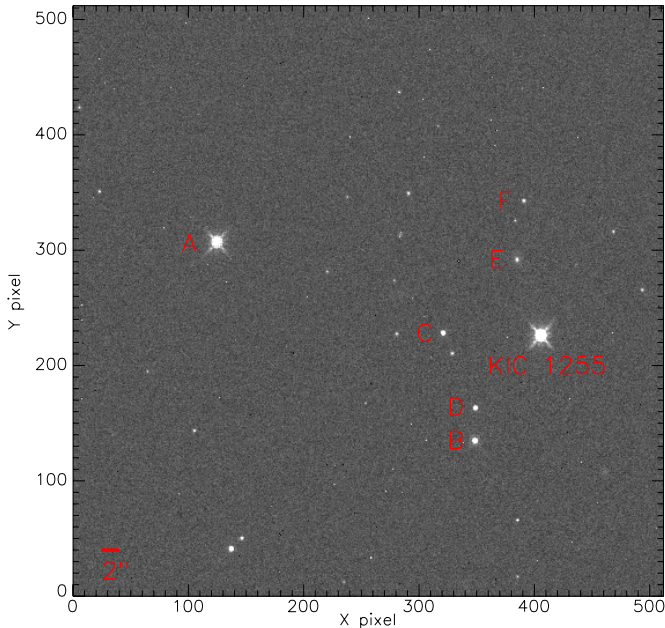
Figure 6. Full frame array of our *HST*/WFC3 1.4 μm photometry. The target star, as well as the handful of nearby reference stars (as listed in Table 2) that we perform photometry on to rule out false positive scenarios, are labeled with letters from A–F.

(A color version of this figure is available in the online journal.)

Figure 7. *HST* F140W filter photometry of various reference stars (listed in Table 2) to KIC 1255. The solid black line denotes the 3σ upper limit on the transit depth obtained by scaling the mean of the short cadence, phase-folded *Kepler* light curve (see Section 2.1).

(A color version of this figure is available in the online journal.)

cycle of ∼19%. Two hundred and fifty-two observations were obtained over the four *HST* orbits, or 63 observations per orbit. We performed aperture photometry, as described above in Section 2.2. We use an aperture radius of 5.75 pixels; we do not subtract the background with an annulus, or otherwise. The results are nearly identical whether we do or do not subtract the background with an annulus with our aperture photometry. The *HST* photometry of KIC 1255 is presented in Figure 3, as well as the best-fit scaled version of the mean short cadence, phase-folded *Kepler* photometry ($g(t)$; Section 2.1); the associated parameters are listed in Table 1. We are unable to detect the transit of KIC 1255 in either our *HST* photometry or the simultaneous *Kepler* photometry (on 2013 February 6). We place a 3σ upper limit on the transit depths on these two occasions of: $A < 0.354$ for our *HST* photometry, and $A < 0.474$ for our *Kepler* Transit 3. We note that the transit of KIC 1255b that we observed with *HST* and *Kepler* happened to be during a stretch of time where the KIC 1255b transit depth was below detectability for a number of transits in a row (∼five days before and after our observed transit).

To rule out whether the transit that we associate with KIC 1255 is actually due to a nearby object, we also perform photometry on all relatively bright stars nearby to KIC 1255 in the *HST* photometry. By using the centroiding analysis methods of (Jenkins et al. 2010) on the *Kepler* photometry of KIC 1255, Rappaport et al. (2012) report that any background source that is causing the transits that we associate with KIC 1255 must be within 2″ of KIC 1255. As we discuss in Section 2.3.2, we rule out sufficiently bright (at least 1% of the flux of KIC 1255) reference stars down to 0″.2 from KIC 1255, and a cursory inspection of Figure 6 indicates there are no sufficiently bright reference stars out to 11″ from KIC 1255. Objects fainter than 1% of KIC 1255, if fully occulted, would not be able to account for the greater than 1% transit depth observed in the *Kepler* photometry. Despite the fact that during our *HST* observations
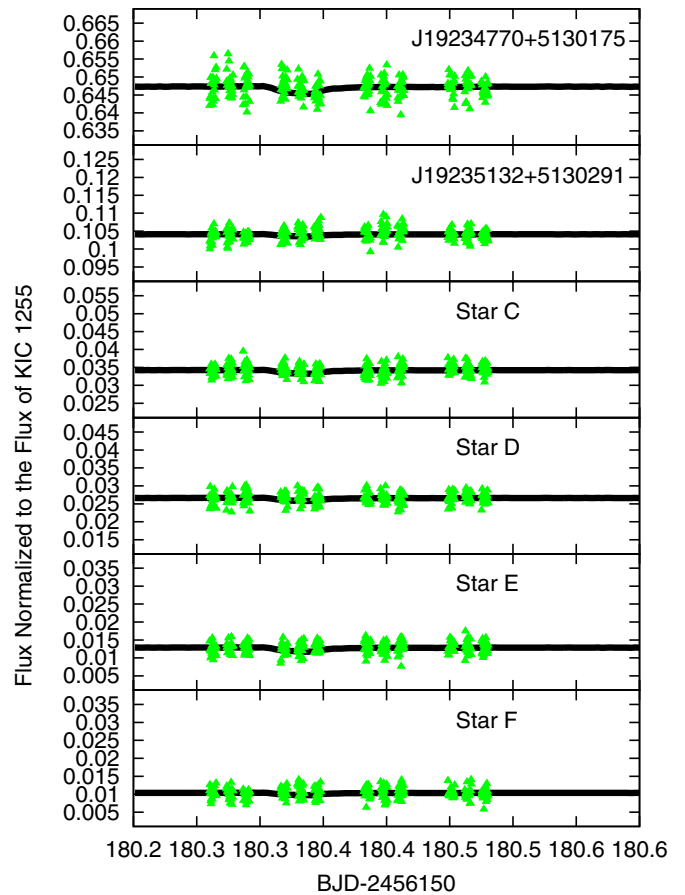
our *HST* and *Kepler* photometry did not display a detectable transit of KIC 1255b, we nevertheless perform photometry on all relatively bright stars that are within 20″ of KIC 1255 and a few select stars of comparable brightness to KIC 1255 that are captured in our *HST* photometry. F140W photometry on all of these stars from orbits 2–5 is presented in Figure 7. We display these stars in Figure 6, which shows the median full-frame image of all of our *HST* F140W photometry. The 3σ upper limits on the transit depth for these stars are given in Table 2. None of these stars displays obvious behavior that would suggest that they serve as a false positive for the characteristic photometry that we associate with KIC 1255b.[21]

2.3.2. HST High Angular Resolution Imaging

HST high angular resolution imaging observations to search for nearby companions to KIC 1255 were obtained with the WFC3 instrument in the following filters in the infrared channel: F125W ($\lambda \sim 1.25$ μm), F140W ($\lambda \sim 1.39$ μm), F160W ($\lambda \sim 1.54$ μm), and the following filters in the ultraviolet and visible channel: F555W ($\lambda \sim 0.531$ μm), F775W ($\lambda \sim 0.765$ μm). We present results of the reduction and analysis of the F555W and F775W channels here.

---

[21] Not that we would necessarily expect them to show such behavior during our *HST* observations, as the KIC 1255b transit was undetectable during these observations.
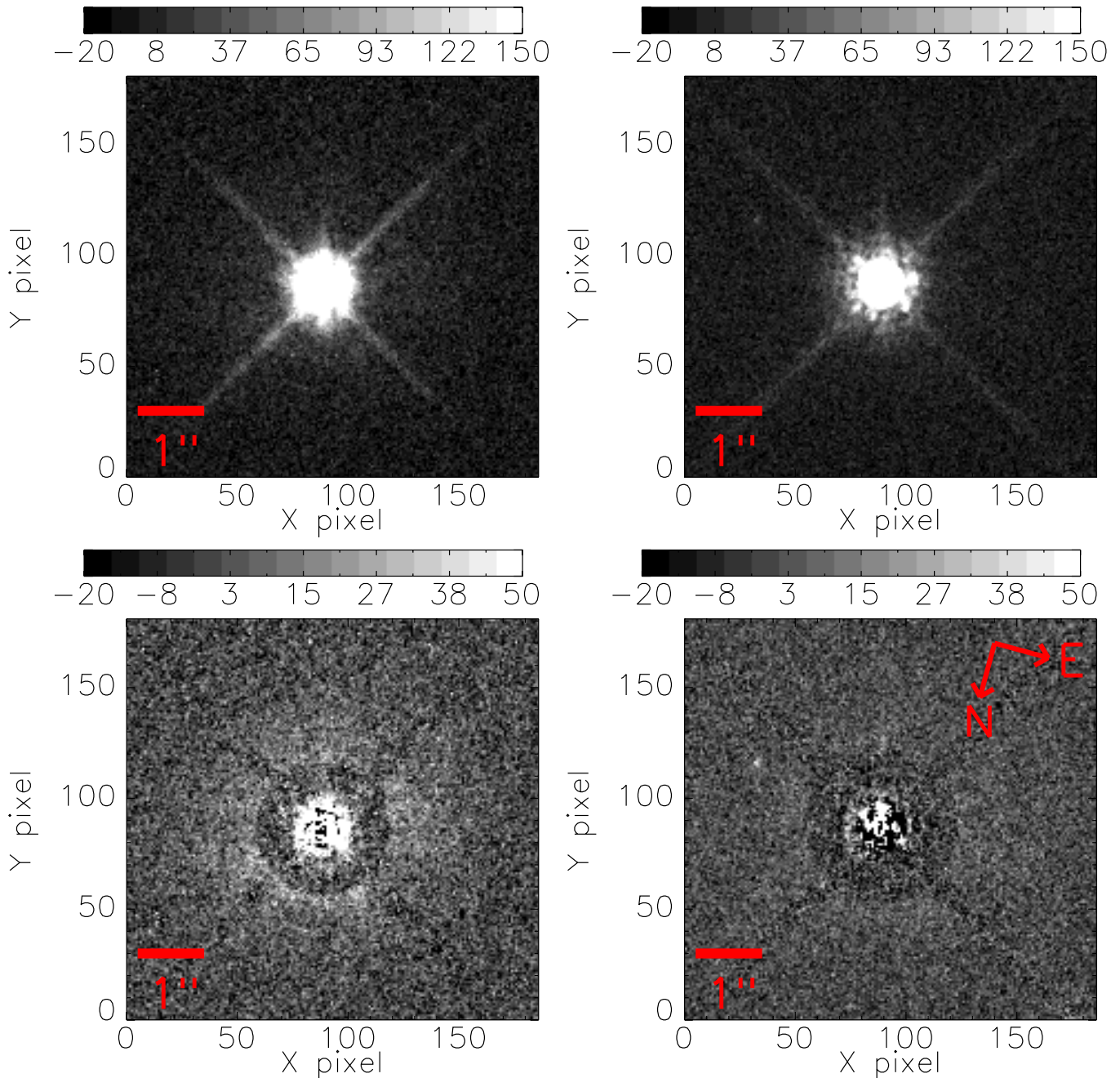
Figure 8. *HST*/WFC3 high angular resolution imaging of KIC 1255 in the F555W channel (left), and the F775W channel (right). The top row of images are the AstroDrizzled images, while the bottom row of images are the PSF subtracted images. For both set of images, the scale is indicated at the top in units of electrons. The compass rose for all panels is given in the lower right panel. For reference, in the F775W difference image (bottom right), the object at 10 o'clock at 2″.2 separation is at a delta-magnitude of 9.1, and is thus too faint to cause the transit we associate with KIC 1255b by a factor of more than ∼50.

(A color version of this figure is available in the online journal.)

Through program GO-12893, which imaged some of *Kepler*'s best Kepler Objects of Interest in terms of small planet candidates on long orbits, we had available F555W and F775W observations of many targets taken with exactly the same dither pattern and essentially the same signal-to-noise. We searched for a subset of the GO-12893 observations for which the target: (1) seemed to be an isolated single star, (2) had a $g - r$ color similar to KIC 1255, and (3) for which the *HST* focus offset matched that for KIC 1255. Visits number 60 (KIC 8150320), 94 (KIC 4139816), and 98 (KIC 5942949) met these criteria and were processed with AstroDrizzle (Fruchter et al. 2010) to the same 0″.0333 scale used for the KIC 1255 images. All

observations consisted of four dithered exposures in which the target was kept just under detector saturation and a fifth exposure at twice saturation to bring up the wings. In each case, the drizzle combination was done to provide a final image well-centered on a pixel. The KIC 1255 direct imaging results are shown in the upper panels of Figure 8 for 460 s in F555W and 330 s in F775W. The combined images had a FWHM of ∼0″.075 and are given in units of electrons.[22]

---

[22] The negative electron values observable in Figure 8 are likely due to the noise in the dark and sky frames that are subtracted to produce the frames seen here.

Table 2
HST Photometry of Reference Stars to KIC 1255

Star Name	Angular Separation from KIC 1255 (″)	A	t_{transit}[a] (BJD-2456150)	y_o	3σ Upper Limit on A	Percentage Brightness of KIC 1255 at $\sim 1.39\,\mu$m
Star A (2Mass J19234770+5130175)	39.15	$0.116^{+0.097}_{-0.084}$	179.969	$-0.35279^{+0.00022}_{-0.00016}$	0.375	64.7
Star B (2Mass J19235132+5130291)	13.40	$0.012^{+0.021}_{-0.011}$	179.969	$-0.89589^{+0.00010}_{-0.00010}$	0.112	10.4
Star C	11.34	$0.052^{+0.053}_{-0.030}$	179.969	$-0.96580^{+0.00010}_{-0.00010}$	0.183	3.4
Star D	10.69	$0.030^{+0.039}_{-0.024}$	179.969	$-0.97340^{+0.00011}_{-0.00011}$	0.158	2.7
Star E	8.39	$0.065^{+0.056}_{-0.043}$	179.969	$-0.98720^{+0.00010}_{-0.00012}$	0.209	1.3
Star F	14.28	$0.009^{+0.018}_{-0.017}$	179.969	$-0.98967^{+0.00010}_{-0.00010}$	0.117	1.0

Notes. [a] We fix t_{transit} to the predicted midpoint of the transit for this analysis.
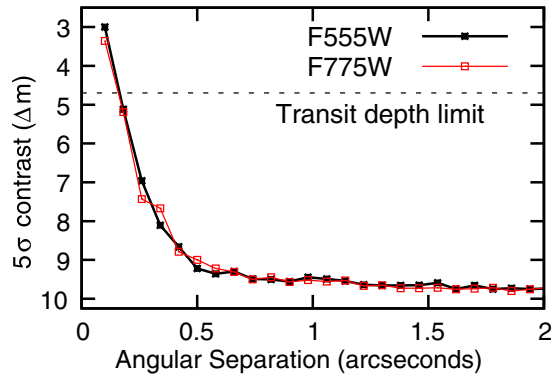

Figure 9. Contrast limits for our *HST*/WFC3 high angular resolution imaging on nearby background/foreground companions to KIC 1255 in difference of magnitude in the F555W channel (red solid line, unfilled squares), and the F775W channel (black solid line, crosses). The horizontal dashed line denotes the limiting magnitude of the faintest object that could produce the transits we associated with KIC 1255b. We rule out companions bright enough to cause the transit we associate with KIC 1255b for separations greater than 0″.2 (5σ).
(A color version of this figure is available in the online journal.)

The observations in the three GO-12893 controls were averaged together to define a point-spread function (PSF) for each filter, then scaled to the intensity of the KIC 1255 images and subtracted to provide the difference images shown in the lower panels of Figure 8, in units of electrons. The subtraction is performed to a radius of 1″.0 at F555W and 1″.2 at F775W; this subtraction is extended to $\sim 3''$ along the diagonal diffraction spikes. For reference, the object at 10 o'clock at 2″.2 separation in Figure 8 of the F775W difference image is at a delta-magnitude of 9.1.

The difference images were used to derive 5σ detection limits as a function of offset distance by evaluating what fluctuations in 3×3 0″.0333 pixels would stand out at this level relative to the scatter in successive 0″.08 annuli starting with one centered at 0″.1 (Gilliland & Rajan 2011). These contrast limits are presented in Figure 9. The *HST* imaging ruled out potential sources of background false positives down to 0″.2 for a delta-magnitude of 4.7 (equivalent to the maximum observed *Kepler* transit depth), thereby reducing the original $2''$ radius area in which these background/foreground candidates could exist by 99% (i.e., <0″.2).

2.4. Keck Adaptive Optics Imaging

We obtained high angular resolution, near-infrared images of KIC 1255 on 2012 May 29 UT using NIRC2 (PI: Keith Matthews) and the Keck II AO system (Wizinowich et al. 2000).

Table 3
Telluric-calibrated Radial Velocities from Keck-HIRES

JD − 2,440,000	Absolute Radial Velocity (km s^{-1})	Uncertainty (km s^{-1})
16020.05982	−36.05	0.10
16028.02128	−36.38	0.10
16076.09278	−36.12	0.10
16110.07628	−36.37	0.10
16532.97013	−36.41	0.10

Observations were acquired in natural guide star mode with the K' filter ($\lambda \sim 2.124\,\mu$m). Given the faintness of KIC 1255 ($R = 15.30$), we opened the deformable mirror loops and applied tip/tilt correction commands only. Images were recorded using the narrow camera mode that provides a 10 mas plate scale. A standard three-point dither pattern was executed to remove background radiation from the sky and instrument optics. A total on-source integration time of 360 s was obtained from six separate frames. Images were processed using standard techniques to replace hot pixel values, flat-field, subtract the background, and align and coadd frames (Crepp et al. 2012).

Figure 10 shows the final reduced image (left panel) along with sensitivity to off-axis sources (right panel). No obvious companions were noticed in either raw or processed frames. Comparing residual scattered light levels to the stellar peak intensity, our NIRC2 observations rule out the presence of possible photometric contaminants at differential flux values comparable to and brighter than the maximum *Kepler* transit depth[23] ($\Delta m = 4.7$), for separations >1″.4 at 3σ.

2.5. Keck Radial Velocities

We obtained five high-resolution spectra of KIC 1255 using High Resolution Echelle Spectrometer (HIRES; Vogt et al. 1994) on the Keck I Telescope to measure absolute RVs. The exposures were 5–10 minutes in duration and achieved signal-to-noise ratios of 12–16 per pixel in *R* band (on blaze). We followed the standard techniques of the California Planet Survey for the reduction and sky subtraction of spectra (Batalha et al. 2011). We measured absolute RVs with the telluric oxygen *A* and *B* bands (759.4–762.1 nm and 686.7–688.4 nm) as a wavelength reference using the method of Chubak et al. (2012). The photon-weighted times of observation, RVs, and errors are listed in Table 3. Individual measurements carry

---

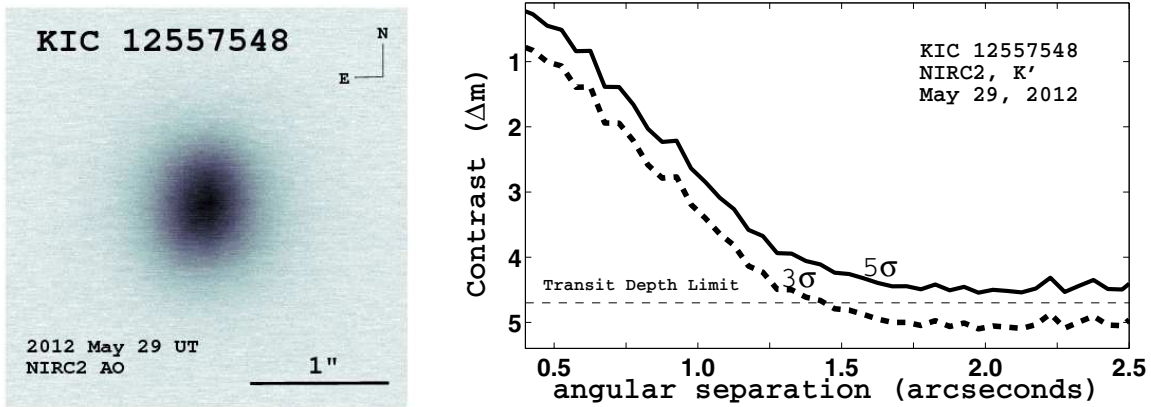[23] See Section 4 for an explanation of why this optical limit ($\Delta m = 4.7$) is likely valid in the near infrared.

Figure 10. Keck/NIRC2 high angular resolution imaging (left) of KIC 1255 in the K' filter ($\lambda_c = 2.124~\mu$m). The associated contrast limits on nearby background/foreground companions to KIC 1255 (right) in difference of magnitude in the K' filter are given with 5σ (solid line) and 3σ confidence (thick dashed line); the thin-dashed horizontal line denotes the limiting magnitude of the faintest object that could produce the transits we associated with KIC 1255b. We rule out companions that bright at this wavelength for separations greater than $1\rlap{.}''4$ (3σ).

(A color version of this figure is available in the online journal.)

0.1 km s^{-1} uncertainties, as demonstrated by bright standard star measurements (Chubak et al. 2012) as well as measurements of faint stars such as Kepler-78 ($V = 12$; Howard et al. 2013).

The RV measurements of KIC 1255 span 512 days and have an rms of 0.17 km s^{-1}. We searched for accelerations in the RV time series that could indicate a stellar mass, long period companion. A linear least squares fit to the data yields a statistically insignificant slope of -0.16 ± 0.90 km s^{-1} yr^{-1}. We then injected artificial RV signals for a hypothetical companion, with a given period, P, and minimum mass, $m \sin i$ (where i is the orbital inclination of the companion), into the data and determined with what confidence we would be able to detect these companions. Zero-eccentricity orbits were assumed and 4000 trials were drawn with a random orbital phase. Inspired by a similar method used by Bean et al. (2010), signals were judged to be detected if the χ^2 of the RV fit after subtracting the mean, $\chi^2_{\rm RV}$, were greater than the χ^2 of a straight line fit, $\chi^2_{\rm straight}$,[24] plus an amount corresponding to 3σ confidence for four degrees of freedom (from our five data-points)—that is, if $\chi^2_{\rm RV} > \chi^2_{\rm straight} + 16.3$. The resulting 50% and 90% confidence limits are given in Figure 11; stronger confidence limits (e.g., 99.73%) result in considerably higher masses, as the time-gaps in the RV data allow for even very massive companions to slip through a small fraction of the time. Also, allowing eccentric orbits would result in less constraining (higher mass) limits at a given orbital period. Our analysis rules out giant planetary-mass companions ($m \sin i \sim 13~M_J$ (Jupiter masses)) for $\lesssim 40$ day orbits, and low-mass stellar companions ($m \sin i \sim 0.2~M_\odot$ or greater) for $\lesssim 10$ yr orbits with 90% confidence.[25] We note an M-dwarf companion with a mass less than $0.2~M_\odot$ would verge on the limit of being too faint to cause the 1% transit depth we associate with KIC 1255.

---

[24] $\chi^2_{\rm straight} = 11.25$ with 4 degrees of freedom.

[25] We note that, if there was an additional companion in the KIC 1255 system (other than the candidate planet), the light-time effect of the host star orbiting around the barycenter of the system (Montalto 2010) would induce periodic variability in the transit timing of the candidate planet. For long period companions, this might manifest itself as long-term variations in the period of the candidate planet; such changes may have been detectable in the *Kepler* data, given the stringent limits on the lack of change in the orbital period reported by Budaj (2013) and van Werkhoven et al. (2014).
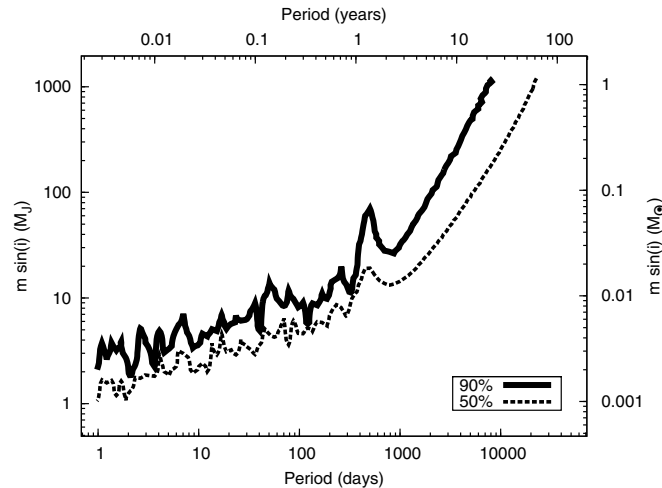

Figure 11. Constraints on the minimum mass, $m \sin i$, and period, P, of possible companions to KIC 1255. These are based on the Keck/HIRES RV measurements that we obtained with telluric-calibrated spectra. Artificial radial velocity signals were injected into the data and were recovered 50% of the time (dashed line) and 90% of the time (solid line) with strong confidence (at a threshold greater than 3σ). We are able to rule out giant planetary mass companions at periods $\lesssim 40$ days and low-mass stellar companions ($m \sin i \sim 0.2~M_\odot$) for $\lesssim 10$ yr orbits with 90% confidence.

2.5.1. Radial Velocity Limit on KIC 1255b's Minimum Mass

Our Keck RV measurements also allow us to attempt to detect, or set an upper limit on, the mass of the candidate planet KIC 1255b. Our Keck RVs phased to the orbital period of KIC 1255b are displayed in Figure 12. Similar to the techniques used above, we then insert circular (zero eccentricity) RV signals at KIC 1255b's orbital period and phase, until these signals exceed the χ^2 limit discussed in Section 2.5. Our 3σ upper limit on KIC 1255b's minimum mass from the Keck RVs is then approximately 1.2 Jupiter-masses ($m \sin i \lesssim 1.2~M_J$), as displayed in Figure 12. We note that, given the sparse RV sampling, allowing eccentric orbits would result in a much higher upper limit on KIC 1255b's minimum mass. Given KIC 1255b's close orbit with its parent star, one would not necessarily expect KIC 1255b to have an eccentric orbit; however, the planet's high mass loss rate suggests a short lifetime for the planet in its present orbit (Perez-Becker & Chiang 2013),
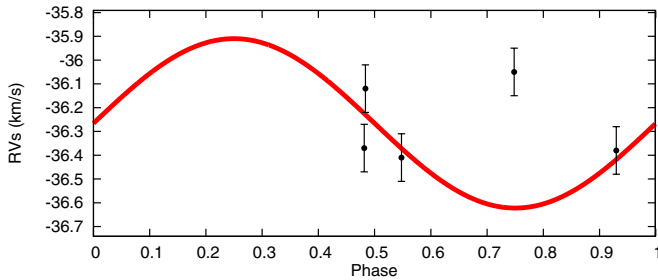
Figure 12. Keck/HIRES RV measurements phased to the orbital period of the candidate planet ($P \sim 0.6536$ days). The red solid line represents the radial velocity fit corresponding to the upper limit on the mass of the candidate planet ($m \sin i \lesssim 1.2\,M_J$) that we can rule out with 3σ certainty, for a circular orbit. (A color version of this figure is available in the online journal.)

leaving open the possibility that the planet's orbit may not have circularized yet.

3. MULTIWAVELENGTH PHOTOMETRIC RESULTS

Our simultaneous *Kepler* ($\sim 0.6\,\mu$m) and CFHT ($\sim 2.15\,\mu$m) photometry, and our simultaneous *Kepler* and *HST* ($\sim 1.4\,\mu$m) photometry, allow us to compare the transit depths from the optical to the near infrared. The ratio of the *Kepler* to the CFHT transit depth is similar in both our first and second CFHT and *Kepler* observations ($A_{\rm Corr}/A_{Kepler} = 0.97 \pm 0.36$ on 2012 August 13 2012 and $A_{\rm Corr}/A_{Kepler} = 1.05 \pm 0.36$ on 2012 September 1 2012). The weighted mean of the A ratio from both observations is $A_{\rm CFHT}/A_{Kepler} = 1.02 \pm 0.20$. For the simultaneous *HST* and *Kepler* observation, we are only able to return a null detection of the transit depth at those wavelengths; the associated ratio of the *HST* to *Kepler* transit depths is $A_{HST}/A_{Kepler} = 0.39 \pm 0.46$. Therefore, we can only say that there is no evidence for strongly different transit depths at these wavelengths. We summarize the ratios at these wavelengths in Table 4.

4. LIMITS ON NEARBY COMPANIONS TO KIC 1255B AND FALSE POSITIVE SCENARIOS

Although we know of no viable binary or higher-order multiple scenario that could explain the unusual photometry we observe for KIC 1255, we note that our high angular resolution imaging, RVs, and multiwavelength photometry place strict limits on companions to KIC 1255 and thus on suggested false positive scenarios.

We searched for nearby companions to KIC 1255 with our *HST*/WFC3 and Keck/NIRC2 high angular resolution imaging. With a maximum transit depth of 1.3% of the stellar flux, the maximum magnitude differential between a background object and KIC 1255 that could be causing the behavior we observe is 4.7 magnitudes. Therefore, our *HST*/WFC3 high angular resolution F555W and F775W ($\lambda \sim 0.765\,\mu$m) imaging[26] is able to rule out companions this bright with 5σ confidence down to $0\rlap{.}''2$ angular separation from KIC 1255b (see Figure 9).

In the near infrared, given the CFHT to *Kepler* transit depth ratio we measure here ($A_{\rm CFHT}/A_{Kepler} = 1.02 \pm 0.20$), we can expect that any object must be no more than 4.7 mag fainter than KIC 1255b at these wavelengths as well; therefore, for our Keck/NIRC2 imaging, we are able to rule out companions this bright down to $1\rlap{.}''4$ separation at 3σ confidence.

---

[26] The F555W ($\lambda \sim 0.531\,\mu$m) and F775W ($\lambda \sim 0.765\,\mu$m) bracket the $\sim 0.6\,\mu$m midpoint of the *Kepler* bandpass.

Table 4
A Ratios for KIC 1255

Data and Transit No.	Ratio
CFHT and *Kepler* Transit 1	$A_{\rm Corr}/A_{Kepler} = 1.05 \pm 0.36$
CFHT and *Kepler* Transit 2	$A_{\rm Corr}/A_{Kepler} = 0.97 \pm 0.24$
CFHT and *Kepler* transits combined	$A_{\rm CFHT}/A_{Kepler} = 1.02 \pm 0.20$
HST and *Kepler* transit	$A_{HST}/A_{Kepler} = 0.39 \pm 0.46$

Our RV observations allow us to rule out low-mass stellar companions ($\sim 0.2\,M_\odot$) for reasonably edge-on orbits, for periods less than 10 yr (this corresponds to $\lesssim 4$ AU using the $0.7\,M_\odot$ stellar mass reported by Rappaport et al. 2012). Our high angular resolution *HST* imaging limit of $0\rlap{.}''2$ corresponds to >94 AU at the ~ 470 parsec distance of KIC 1255 quoted by Rappaport et al. (2012). We therefore note there is little viable parameter space (only companion separations, s, of 4 AU $\lesssim s \lesssim 94$ AU remain viable) for a binary or higher-order multiple companion to KIC 1255b that could be masquerading as a false positive for the photometry of KIC 1255 that we associate with a disintegrating low-mass planet.

Lastly, we note that the fact that our near-infrared and optical photometry report similar transit depth, also allows us to place an additional constraint on hierarchical triple or background binary configurations with stars of different spectral types. For instance, if the photometry we associate with KIC 1255b was somehow due to a pair of late M-dwarfs (an effective temperature of $T_{\rm eff} \sim 3000$ K) eclipsing one another, whose light was diluted by the K-dwarf star KIC 1255 ($T_{\rm eff} \sim 4400$ K; Rappaport et al. 2012), the $\sim 1\%$ optical transit depths would result in $\sim 6\%$ transit depths at $2.15\,\mu$m, a depth we can rule with very high confidence ($\sim 25\sigma$). Similar limits could be set on a background binary that is of a different spectral type from KIC 1255. A background binary of similar spectral type to KIC 1255 remains a possible false positive; however, it is unclear how such a scenario would explain the variable transit depths and asymmetric transit profile we observe with this candidate planet.

With these stringent limits on false positive scenarios, we therefore conclude that the disintegrating low-mass planet scenario is the simplest explanation suggested to date for the *Kepler* photometry, and our multiwavelength photometry, RVs, and high angular resolution imaging.

5. DISCUSSION

5.1. Size of Grains in the Dust Tail of KIC 1255b

The wavelength dependence of extinction by dust grains can provide information on their size and, in some cases, their composition (e.g., for interstellar grains see Mathis et al. 1977). This is due to the fact that the efficiency of scattering generally diminishes as the observational wavelength approaches the approximate particle circumference (Hansen & Travis 1974). For this reason, the nearly identical transit depths we measure at $\lambda \sim 0.6\,\mu$m with *Kepler* and at $\lambda \sim 2.15\,\mu$m with CFHT/WIRCam allow us to set a lower limit on the largest particles in the hypothetical dust tail trailing KIC 1255b. We set this lower limit on the size assuming that all of the dust particles are a single, identical size in Section 5.1.3 and for a distribution of particle sizes in Section 5.1.4.

5.1.1. Spectral Dependence of Extinction

The extinction (scattering plus absorption) of light by dust grains is a function of the wavelength, λ, of the light, the size
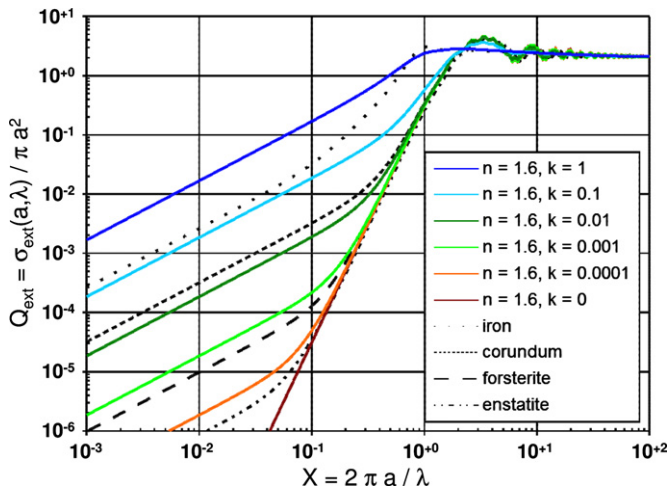
Figure 13. Extinction efficiency, Q_{ext} (Mie extinction cross sections, normalized to the geometric area of the grain), as a function of the nondimensional grain size parameter, $X = 2\pi a/\lambda$, where a is the radius of the grain, and λ is the wavelength of observation. The dotted, short-dashed, long-dashed, and dot-dashed lines indicate the extinction efficiency of iron, corundum, forsterite, and enstatite, as calculated as described in the text.

(A color version of this figure is available in the online journal.)

of the grains, denoted by the grain radius, a, and the complex index of refraction of the dust material, where n denotes the real component and k the imaginary component. While there is also some dependence of extinction upon the shape of the dust grains, for simplicity, we will only consider spherical grains here and employ the Mie algorithm presented by Bohren & Huffman (1983) to calculate their cross sections. Figure 13 plots the extinction efficiency (the ratio of the extinction cross section to the geometric cross section), $Q_{ext}(a, \lambda) = \sigma_{ext}(a, \lambda)/(\pi a^2)$, as a function of the nondimensional size, $X = 2\pi a/\lambda$, for grains with $n = 1.6$ and $k = 0$ (no absorption) and k varying from 0.0001 (low absorption) to 1 (highly absorbing).

We note that, for large grains ($X \gg 1$; the right-hand side of the plot), the extinction cross section is approximately constant ($Q_{ext}(a, \lambda) = \sigma_{ext}(a, \lambda)/(\pi a^2) \to 2$) and only slightly dependent on wavelength, regardless of the absorption, k. For wavelengths longer or approaching the approximate particle circumference (the left side of the plot), the amount of extinction nominally depends on the amount of absorption (e.g., van de Hulst 1981). Nonetheless, even for a great deal of absorption (i.e., $k = 1$; the dark blue line in Figure 13), the extinction cross section falls sharply for wavelengths longer than the approximate particle circumference[27]; for low levels of absorption or none at all (the light green, orange, and red lines in Figure 13), the fall off is even steeper.[28] The asymptotic limits apparent in the plot are listed in Table 5. Therefore, we surmise, based on the nearly equal *Kepler* and CFHT transit depths, and thus the near equal levels of extinction between these two wavelengths, that our observations probe the right hand side of the plot; we can therefore set a lower limit on the largest particles in the hypothetical dust tail trailing KIC 1255b.

For the scattering calculations that follow, we assume typical values for the complex index of refraction, n and k, based on the values for typical Earth-abundant refractory materials, such as olivines and pyroxenes. Across our wavelength range

Table 5
Wavelength Extinction and Sensitivity Limits

Parameter Region	σ_{ext} (a, λ)	α $(a, \lambda_1, \lambda_2)$
$a \gg \lambda/2\pi$	$2\pi a^2$	0
$a \ll \lambda/2\pi$ and $k = 0$	$\propto a^6/\lambda^4$	4
$a \ll \lambda/2\pi$ and $k \neq 0$	$\propto a^3/\lambda$	1

of interest ($\lambda = 0.6$ to 2.15 μm), for these materials, the imaginary component of the index of refraction is typically small, $k \lesssim 0.02$, while the real component of the index of refraction is often approximately $n \sim 1.6$ (Kimura et al. 2002 and references therein). We also repeat our scattering calculations for a number of materials that have previously been suggested to be responsible for the dust supposedly trailing KIC 1255b. Four such materials, suggested by Budaj (2013), are forsterite (Mg_2SiO_4; a silicate from the olivine family), enstatite ($MgSiO_3$; a pyroxene without iron), pure iron, and corundum (Al_2O_3; a crystalline form of aluminum oxide). Three of these materials have similar complex indices of refraction across our wavelength range of interest ($\lambda = 0.6$ to 2.15 μm): that is, $n \sim 1.6$ and $k < 10^{-4}$ for enstatite (Dorschner et al. 1995), $n \sim 1.6$ and $k < 10^{-3}$ for forsterite (Jager et al. 2003), and $n \sim 1.6$ and $k < 0.04$ for corundum (Koike et al. 1995). Pure iron is an outlier with $n \sim 2.9$–3.9 and $k \sim 3$.–7.0 (Ordal 1988) for wavelengths from $\lambda = 0.6$ to 2.15 μm. In Figure 13, we also display the resulting extinction efficiency, $Q_{ext}(a, \lambda)$, of these materials.[29]

5.1.2. Extinction Wavelength Dependence

To parameterize the amount of extinction between our two wavelengths, λ_1 and λ_2, we employ the Ångström exponent, $\alpha(a, \lambda_1, \lambda_2)$, a measure of the dependence of extinction on wavelength,[30] defined as follows:

$$\alpha(a, \lambda_1, \lambda_2) \equiv -\frac{\log\left[\sigma_{ext}(a, \lambda_2)/\sigma_{ext}(a, \lambda_1)\right]}{\log(\lambda_2/\lambda_1)}. \quad (2)$$

The ratio of the transit depths in Table 4 is approximately the ratio of the extinctions at these two wavelengths, $\sigma_{ext}(a, \lambda_2)/\sigma_{ext}(a, \lambda_1) = 1.02 \pm 0.20$. Therefore, the associated value of $\alpha(a, 0.6\,\mu\text{m}, 2.15\,\mu\text{m}) = -0.02$ with ranges -0.16 to $0.16\,(1\sigma)$, -0.27 to $0.37\,(2\sigma)$, and -0.38 to $0.68\,(3\sigma)$.

5.1.3. Single Size Grains

What is the maximum size of particles in the hypothetical dust tail of KIC 1255b if the tail is composed solely of single size spherical particles? Figure 14 plots Mie calculations of $\alpha(a, 0.6\,\mu\text{m}, 2.15\,\mu\text{m})$ for grains with $n = 1.6$, $k = 0.02$, and radius a. The 1σ, 2σ, and 3σ error bars on $\alpha(a, 0.6\,\mu\text{m}, 2.15\,\mu\text{m})$ are displayed with the dashed orange, green, and blue lines, respectively, in Figure 14. Therefore, for a dust tail consisting of single size grains, their radius would have to be $\gtrsim 0.5\,\mu$m (3σ).

---

[27] For $k \neq 0$, the extinction can be approximated by $\sigma_{ext}(a, \lambda)/\pi a^2 \propto k X$.

[28] For $k \equiv 0$, the extinction can be approximated by $\sigma_{ext}(a, \lambda)/\pi a^2 \propto X^4$, a relation found by Rayleigh (1871). For $k \neq 0$, there may be a transition region between the two extremes where $\sigma_{ext}(a, \lambda)/\pi a^2 \propto X^4$.

---

[29] The curves presented in Figure 13 represent averages of the extinction efficiency, Q_{ext}, for wavelengths of 0.6, 1.0, 1.6, 2.0, and 2.15 μm (except for iron, which omits the 0.6 μm calculation because it is below the tabulated index of refraction values), using index of refraction values for enstatite from Dorschner et al. (1995), forsterite from Jager et al. (2003), corundum from Koike et al. (1995), and iron from Ordal (1988).

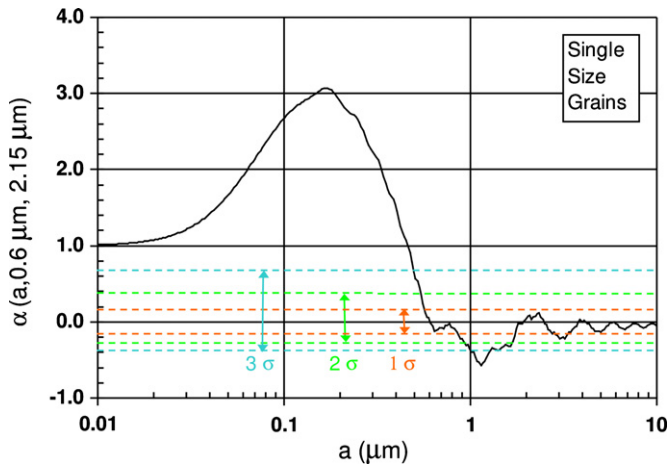[30] Defined by Ångström (1929) in the context of dust in the Earth's atmosphere.

Figure 14. Plot of the Ångström exponent for spherical grains of radius, a. We assume an index of refraction of $n = 1.6$ and an imaginary component of the index of refraction of $k = 0.02$. The horizontal orange, green, and blue dashed lines show the 1σ, 2σ, and 3σ limits on $\alpha(a, \lambda_1, \lambda_2)$, respectively, from Section 5.1.2. Grains of a single size have to be larger than $a \gtrsim 0.5\,\mu$m (3σ) to be consistent with the ratio of our CFHT/WIRCam and *Kepler* transit depths.

(A color version of this figure is available in the online journal.)

We have also reproduced these scattering calculations for four materials that have been suggested to make up the particles trailing KIC 1255b (these are corundum, pure iron, forsterite, and enstatite) rather than for our hypothetical $n = 1.6$ and $k = 0.02$ material. Due to the close agreement between the complex index of refraction of forsterite, enstatite, and corundum, and our assumed $n = 1.6$ and $k = 0.02$ values, the size limit on single-sized forsterite, enstatite, or corundum particle is indistinguishable from our hypothetical material; that is, such grains must be $\gtrsim 0.5\,\mu$m (3σ confidence). Pure iron, on the other hand, which has a complex index of refraction that differs significantly from the above values, results in a less stringent limit on single size iron particles; pure iron particles would have to be $\gtrsim 0.2\,\mu$m (3σ). However, due to iron's high vapor pressure,[31] we find it doubtful that pure iron particles could survive the high temperatures of a dust tail trailing KIC 1255b in the first place without sublimating. We therefore quote only our $\gtrsim 0.5\,\mu$m (3σ) size limit on single size particles, henceforth.[32]

5.1.4. Grain Size Distributions

We concede that a distribution consisting only of a single size of grain may not be the most realistic assumption for the hypothetical grains trailing KIC 1255b. Therefore, we also consider a range of particle sizes. Specifically, we consider grains with a specific particle size distribution denoted by a power law with slopes, ν, formally defined below. Power law size distributions have been used in a diverse range of applications, for example: to model interstellar dust grains ($\nu \sim 3.3$–3.6; Mathis et al. 1977; Bierman & Harwit 1980), large particles in the comas of comets ($\nu \sim 4.7$ for particles

---

[31] Iron has a vapor pressure $\sim$50 times greater than that for olivines (Perez-Becker & Chiang 2013). The survival of olivines have already been called into question at the extreme $\sim$2000 K temperatures expected in the tail trailing KIC 1255b (Rappaport et al. 2012).
[32] Obviously, if the grains in the putative tail trailing KIC 1255b are composed of a material with very different optical properties than what we have assumed—$n \sim 1.6$ with a small k ($\lesssim 0.1$)—this could result in a different minimum size than we have presented here. We are unaware of a material that is likely to be present trailing KIC 1255b with very different optical properties than what we have assumed and that is likely to survive the high temperatures in the tail trailing KIC 1255b without sublimating.

1 μm to 1 *mm* in size for the comet 103P/Hartley 2; Kelley et al. 2013), and dust (aerosols) in the Earth's lower atmosphere from a world-wide network of ground-based Sun photometers ($3 \leqslant \nu \leqslant 5$; Liou 2002; Holben et al. 1998).

We consider a distribution of grains ranging in size from $a = a_{\min}$ to $a_{\max}$. Let $N(a)$ be the number density of grains per unit grain radius and per unit area of the column along the path connecting the observer to the star. The average extinction cross section for the distribution, $\overline{\sigma}_{\rm ext}(a_{\min}, a_{\max}, \lambda)$, is given by

$$\overline{\sigma}_{\rm ext}(a_{\min}, a_{\max}, \lambda) = \frac{\int_{a_{\min}}^{a_{\max}} N(a')\,\sigma_{\rm ext}(a', \lambda)\,da'}{\int_{a_{\min}}^{a_{\max}} N(a')\,da'}, \qquad (3)$$

where the overbar indicates the normalized average over the grain size distribution. The definition of Ångström exponent is readily adapted to distributions by replacing $\sigma_{\rm ext}(a, \lambda)$ with $\overline{\sigma}_{\rm ext}(a_{\min}, a_{\max}, \lambda)$ in Equation (2):

$$\begin{aligned}
&\alpha(a_{\min}, a_{\max}, \lambda_1, \lambda_2) \\
&\equiv -\frac{\log\left[\overline{\sigma}_{\rm ext}(a_{\min}, a_{\max}, \lambda_2)/\overline{\sigma}_{\rm ext}(a_{\min}, a_{\max}, \lambda_1)\right]}{\log(\lambda_2/\lambda_1)}.
\end{aligned} \qquad (4)$$

Likewise, the first and second columns in Table 5 are readily adapted for size distributions by replacing a by $\overline{a}$, a^2 by $\overline{a^2}$, and so on.

We now specialize to the case of a power law distribution. We define the number density of particles of a given size as follows: $N(a) = c\,a^{-\nu}$ for $a_{\min} \leqslant a \leqslant a_{\max}$, where the particle size distribution parameter, ν, taken to lie between $1 \leqslant \nu \leqslant 5$, and c, is a normalization constant.[33] In the following, we arbitrarily set the minimum particle size to be $a_{\min} = 0.01\,\mu$m, and set the maximum particle size to lie in an astrophysically plausible range of $0.01\,\mu$m $\leqslant a_{\max} \leqslant 10\,\mu$m. We calculate $\alpha(a_{\min} = 0.01\,\mu$m, $a_{\max}, \nu, 0.6\,\mu$m, $2.15\,\mu$m) for spherical grains comprised of material having $n = 1.6$ and $k = 0.02$, and plot the results in Figure 15. We note the similarity of this plot to the one for a single-sized particle in Figure 14.[34]

The implication is that there needs to be a sufficient proportion of grains with $a \gtrsim 1\,\mu$m for the ratio of the extinctions at the two wavelengths to be so close to 1. In the case of a power law grain size distribution, this requires both a sufficiently large upper size cutoff, $a_{\max}$, and a sufficiently small power law slope, ν. Note that, in this limit, the specific value of the imaginary component of the index of refraction, k, makes little difference.

At this point, we note the important caveat that the wavelength sensitivity as defined in Equation (2) or 4 implicitly assumes that the dust tail is optically thin. The numerator in Equation (3) is the optical thickness, $\tau(\lambda)$, through the dust tail. Using the fact that the transmission $T(\lambda) \equiv \exp[-\tau(\lambda)]$ and that the extinction is $1 - T(\lambda)$, we find that in the optically thin limit, i.e., where $\tau(\lambda) \ll 1$:

$$1 - T(\lambda) \rightarrow \overline{\sigma}_{\rm ext}(a_{\min}, a_{\max}, \lambda) \times \int_{a_{\min}}^{a_{\max}} N(a')\,da'$$
$$\text{if } \tau(\lambda) \ll 1. \quad (5)$$

---

[33] Incidentally, for aerosols in the Earth's atmosphere, Junge (1963) showed that ν and α were simply related. An analytic demonstration using a simple approximation is presented by DeVore (2011).
[34] As $a_{\max} \rightarrow 0.01\,\mu$m, $\alpha(a_{\min}, a_{\max}, \nu, \lambda_1, \lambda_2) \rightarrow 1$ for all values of ν. As $a_{\max}$ increases beyond $\sim 1\,\mu$m, $\alpha(a_{\min}, a_{\max}, \nu, \lambda_1, \lambda_2)$ approaches a constant that depends upon ν. As ν decreases, the proportion of large particles increases and the constant value approaches 0. In between these two limits, $\alpha(a_{\min}, a_{\max}, \nu, \lambda_1, \lambda_2)$ has a maximum in the range between roughly 2 and 3.
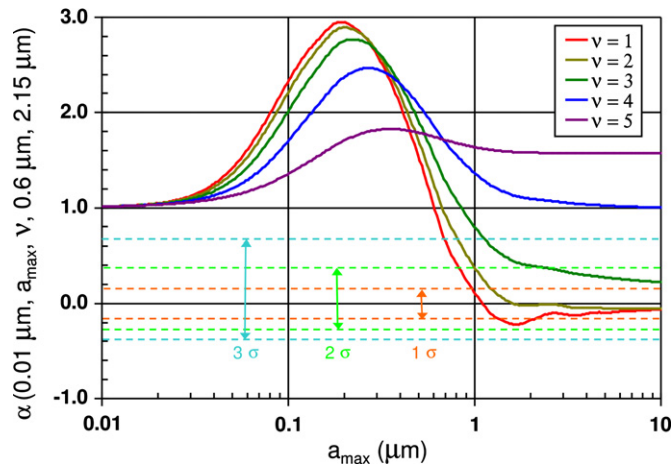
Figure 15. Plot of extinction sensitivity for a range of particle size distributions with $\nu = 1, 2, 3, 4,$ and 5. We employ an index of refraction of $n = 1.6$, an imaginary component of the index of refraction, $k = 0.02$, and calculate the particle distribution between a minimum radius of $a_{min} = 0.01 \, \mu m$ and a maximum radius of $0.01 \leqslant a_{max} \leqslant 10 \, \mu m$. The horizontal orange, green, and blue dashed lines show the 1σ, 2σ, and 3σ limits on $\alpha(a_{min}, a_{max}, \nu, \lambda_1, \lambda_2)$, respectively, from Section 5.1.4. Only smaller power law slopes, and thus particle size distributions with more large particles, e.g., $\nu = 1, 2,$ and 3, result in a sufficient number of near micron-sized grains and thus satisfy the ratio of our CFHT/WIRCam and *Kepler* transit depths at the 3σ level.

(A color version of this figure is available in the online journal.)

Since the integral on the right in Equation (5) is independent of λ, extinction is proportional to $\overline{\sigma}_{ext}(a_{min}, a_{max}, \lambda)$ in this limit. However, since it is likely that the putative dust tail does not obscure the entire stellar surface, there may be portions of the tail where the dust is optically thick, i.e., $\tau(\lambda) \gtrsim 1$. To the extent that this is the case, the extinction measurements will tend to give the same value independent of λ, the assumptions underlying $\alpha(\lambda_1, \lambda_2)$ break down, and the utility of $\alpha(\lambda_1, \lambda_2)$ for inferring grain size diminishes.

5.1.5. The Impact of Large Particles on the Supposed Forward Scattering Peak

The presence of an increase in flux immediately preceding the dip attributable to strong forward scattering (Rappaport et al. 2012; Brogi et al. 2012; Budaj 2013) is also suggestive of large particles, since the strength of forward scattering is a strong function of grain size (e.g., DeVore, et al. 2013). We note that, according to the model of Budaj (2013), there may be some tension between our finding of $a \gtrsim 0.5 \, \mu m$ particles and the *Kepler* observations, as $0.1–1.0 \, \mu m$ particles arguably overpredict the amount of forward scattering compared to the *Kepler* observations.[35] However, the forward scattering increase also suggests that the dust responsible is not optically thick since scattering acts both to inhibit the forward-scattered photons as well as cause the flux to diverge angularly. If multispectral measurements of the forward-scattering peak were obtained with adequate signal-to-noise, then they could be used to provide information on grain size through the strong dependence of the angular spread of forward scattering on the ratio of the effective grain diameter to the wavelength.

5.2. KIC 1255b Particle Lifting

If the largest particles in the tail of KIC 1255b are at least $0.5 \, \mu m$ in size, then this raises the question of how such large particles were lofted from the planet in the first place. According to the hydrodynamic wind model of Perez-Becker & Chiang (2013), the present-day mass of KIC 1255b is $\lesssim 0.02 \, M_\oplus$, or less than half the mass of Mercury. Only for masses this small are surface gravities weak enough to allow evaporative winds to blow with mass-loss rates satisfying the observations. These authors have already shown that spherical grains having radii of $1 \, \mu m$ and bulk densities of $3 \, g \, cm^{-3}$ could be dragged by winds outside the Roche lobe of KIC 1255b, albeit only marginally if the planet mass is near its upper limit. As the planet radius shrinks, the sizes of particles that can escape grow in inverse proportion (see their Equation (30) and surrounding discussion). In sum, as long as the planet is small enough, micron-sized or larger particles can escape. Therefore, our observations suggest that the candidate planet KIC 1255b might best be described as a sub-Mercury, rather than super-Mercury, mass planet.

Note that the particles do not need to be lifted directly from the planetary surface, since the grains only condense at an altitude where the wind has an opportunity to cool adiabatically. Indeed, the grains cannot be present at their maximum abundance (relative to gas) at the base of the wind; if they were, the flow would be so optically thick that the planetary surface would be shielded from starlight and would not heat to the temperatures required for an evaporative wind to be launched.[36] In the wind solutions of Perez-Becker & Chiang (2013), the dust abundance increases by orders of magnitude from the surface to the Roche lobe (see their Figure 3). Thus, the problem of lifting grains beyond the Roche lobe should only be a problem near the Roche lobe, and it is there that Perez-Becker & Chiang (2013) compare the drag force exerted by the wind with the planet's tidally modified gravity. We suppose it is possible that the problem of lift can be avoided altogether if grains condense outside the Roche lobe. We cannot rule this possibility out since the grain condensation profile was merely parameterized by Perez-Becker & Chiang (2013), not solved from first principles.

5.3. Prospects for Follow-up Observations

The enlightening multiwavelength observations presented in this paper were greatly facilitated by the impressive photometric capabilities of the *Kepler* spacecraft that allowed us to achieve simultaneous, accurate optical photometry, in addition to our ground- and space-based photometry and imaging. With the recent malfunction of this spacecraft, prospects for illuminating followup studies of this object are much dimmer than previously and may require much the more difficult task to schedule follow up from several telescopes simultaneously.

Although the KIC 1255b transit does not appear to be strongly wavelength dependent from $0.6–2.15 \, \mu m$, follow-up observations further into the infrared would be expected to show transit depth differences compared with those obtained simultaneously in the optical, unless the size of particles in the cometary tail are several microns in size. Such observations

---

[35] Other possibilities include the suggestion that the cometary tail might be composed of different sized particles at different distances from the planet, as suggested by Budaj (2013), or that the tail might be composed of particles with different scattering properties than we would naively expect.

[36] In principle, the surface could be heated to about 1800 K by radiation emitted from dusty layers at altitude but such a surface temperature would still be too low for the planet to emit a wind of the required strength to match observations. Heat redistribution by winds and gravity waves across the day–night terminator would only lower the surface temperature; see Budaj et al. (2012) and Perez-Becker & Showman (2013).

could be obtained with the *Spitzer*/IRAC (Fazio et al. 2004) instrument. We note that several micron-sized particles would be inconsistent with the size of the forward-scattering peak observed with *Kepler* (Rappaport et al. 2012; Budaj 2013; unless there is evolution of the grain sizes along the tail). Low-resolution spectroscopy over a wide spectral range, either from the ground or from space, would be useful to look for both wavelength-dependent transit depth changes and morphological changes in the photometry of the dust tail as revealed by the forward-scattering peak and asymmetric egress of the transit. We note that the strength of the forward-scattering peak is also expected to be wavelength dependent, and observations with sufficient precision to look for such minute changes would be highly illuminating.

6. CONCLUSIONS

We have presented multiwavelength photometry, high angular resolution imaging, and RVs of the intriguing disintegrating low-mass candidate planet, KIC 1255b. We summarize our findings as follows.

1. *Comparison of our CFHT/WIRCam 2.15 μm to Kepler 0.6 μm transit depths and the resulting constraints on particle sizes in the tail trailing KIC 1255b:* The average ratio of the transit depths that we observe from the ground with CFHT/WIRCam and space with *Kepler* at our two epochs are 1.02 ± 0.20. In the disintegrating planet scenario, the only way to see a lack of extinction from the optical to the near infrared is if the circumference of the particles are at least approximately the wavelength of the observations. Therefore, if the transits we observe are due to scattering from single size particles streaming from the planet in a comet-like tail, then the particles must be ~ 0.5 μm in radius or larger.[37] Similarly, if the particle size distribution in the tail follows a number density defined by a power law, then only smaller power law slopes, and thus larger particle sizes, result in a sufficient number of near micron-sized grains to satisfy our observations.

2. *Comparison of our HST 1.4 μm and Kepler 0.6 μm null detections:* Unfortunately, we were unable to detect the transit of KIC 1255b in our simultaneous *HST* and *Kepler* photometry, due to the fact that the transits of KIC 1255b had largely disappeared in the *Kepler* photometry for $\sim$five days before and after our observed transit. We are therefore able to conclude little from these observations, other than there is no evidence for strongly different transit depths at these wavelengths.

3. *Particle lifting from KIC 1255b:* Perez-Becker & Chiang (2013) have already demonstrated that lifting particles nearly a micron in size is possible from KIC 1255b. As lifting such large particles becomes much more difficult as one increases the mass of the candidate planet, we note our $\gtrsim 0.5$ μm limit on single-sized particles in the tail trailing KIC 1255b favors a sub-Mercury, rather than super-Mercury, mass for KIC 1255b.

4. *Constraints on false positives from our high angular resolution imaging, RVs, and photometry:* Our *HST* (~ 0.53 μm and ~ 0.77 μm) high angular resolution imaging allows us to rule out background and foreground candidates at angular separations greater than $0''.2$ that could be responsible for the transit we associate with a planet transiting KIC 1255b. The associated limit from our ground-based Keck/NIRC2 AO observations in K' band (~ 2.12 μm) is for separations greater than $1''.4$. Our RV observations allow us to rule out low-mass stellar companions ($\gtrsim 0.2$ $M_\odot$) for periods less than $\lesssim 10$ yr, and 13 Jupiter-mass companions for periods less than $\lesssim 40$ days. Furthermore, the similar transit depths we observe in the near infrared with CFHT/WIRCam and in the optical with *Kepler* also allow us to rule out background/foreground candidates, or higher-order multiples with significantly different spectral types, as this would result in a color-dependent transit depth from the optical to the near infrared. Although prior to these observations, we knew of no viable false positive scenario that could reproduce the unique photometry we observed with *Kepler* (e.g., the forward scattering bump before transit, the sharp ingress and gradual egress transit profile, the sharply varying transit depths), we note that we have now greatly reduced the parameter space for viable false positive scenarios. We conclude that the disintegrating low-mass planet scenario is the simplest explanation for our multi-wavelength photometry, RVs, and high angular resolution imaging suggested to date.

5. *Limit on the mass of the candidate planet KIC 1255b:* Our KECK/HIRES RVs of KIC 1255b allow us to place an upper limit on the minimum mass of the candidate planet that confirms it is firmly in the planetary regime; this limit is $m \sin i \lesssim 1.2$ M_J with 3σ confidence, assuming a circular orbit.

---

[37] We note this is in some disagreement, and modest agreement, with two efforts that presented scattering models compared to the *Kepler* photometry. The findings of Brogi et al. (2012) modestly disagree with our own, as they suggest the particles in the tail trailing KIC 1255b must have a typical grain size of 0.1 μm from six quarters of long cadence *Kepler* photometry. The results of Budaj (2013) are in modest agreement with our own, as their analysis of 14 quarters of *Kepler* long- and short-cadence photometry suggest grain sizes from 0.1 to 1.0 μm.

REFERENCES

Ångström, A. 1929, Geogr. Ann., 11, 156
Batalha, N. M., Borucki, W. J., Bryson, S. T., et al. 2011, ApJ, 729, 27
Bean, J. L., Seifahrt, A., Hartman, H., et al. 2010, ApJL, 711, L19
Bierman, P., & Harwit, M. 1980, ApJ, 241, L105
Bohren, C. F., & Huffman, D. R. 1983, Absorption and Scattering of Light by Small Particles (New York: Wiley)
Borucki, W. J., Koch, D., Jenkins, J., et al. 2009, Sci, 325, 709
Brogi, M., Keller, C. U., de Juan Ovelar, M., et al. 2012, A&A, 545, L5
Budaj, J. 2013, A&A, 557, A72
Budaj, J., Hubeny, I., & Burrows, A. 2012, A&A, 537, A115
Chubak, C., Marcy, G., Fischer, D. A., et al. 2012, arXiv:1207.6212
Crepp, J. R., Johnson, J. A., Howard, A. W., et al. 2012, ApJ, 761, 39
Croll, B. 2006, PASP, 118, 1351
Croll, B., Albert, L., Lafreniere, D., Jayawardhana, R., & Fortney, J. J. 2010a, ApJ, 717, 1084
Croll, B., Jayawardhana, R., Fortney, J. J., Lafrenière, D., & Albert, L. 2010b, ApJ, 718, 920
DeVore, J. G. 2011, JAtOT, 28, 779
DeVore, J. G., Kristl, J. A., & Rappaport, S. A. 2013, JGR, 118, 5679
Dorschner, J., Begemann, B., Henning, T., Jaeger, C., & Mutschke, H. 1995, A&A, 300, 503
Dressel, L., Wong, M., Pavlovsky, C., Long, K., et al. 2010, Wide Field Camera 3 Instrument Handbook, Version 2.1 (Baltimore, MD: STScI)
Fazio, G. G., Hora, J. L., Allen, L. E., et al. 2004, ApJS, 154, 10
Fruchter, A. S., Hack, W., Dencheva, N., Droettboom, M., & Greenfield, P. 2010, in STScI Calibration Workshop Proceedings, ed. S. Deustua & C. Oliveira (Baltimore, MD: STScI), 376
Gilliland, R. L., & Rajan, A. 2011, Instrument Science Report WFC3 2011-03 (Baltimore, MD: STScI)

Hansen, J. E., & Travis, L. D. 1974, SSRv, 16, 527
Holben, B., Eck, T. F., Slutsker, I., et al. 1998, RSEnv, 66, 1
Howard, A. W., Sanchis-Ojeda, R., Marcy, G. W., et al. 2013, Natur, 503, 381
Jager, C., Dorschner, J., Mutschke, H., et al. 2003, A&A, 408, 193
Jenkins, J. M., Borucki, W. J., Koch, D. G., et al. 2010, ApJ, 724, 1108
Junge, C. E. 1963, Air Chemistry and Radioactivity (New York: Academic Press)
Kawahara, H., Hirano, T., Kurosaki, K., Ito, Y., & Ikoma, M. 2013, ApJL, 776, L6
Kelley, M. S., Lindler, D. J., Bodewits, D., et al. 2013, Icar, 222, 634
Kimura, H., Mann, I., Biesecker, D. A., & Jessberger, E. K. 2002, Icar, 159, 529
Kipping, D. M. 2010, MNRAS, 408, 1758
Koike, C., Kaito, C., & Yamamoto, T. 1995, Icar, 114, 203
Liou, K. N. 2002, An Introduction to Atmospheric Radiation (2nd ed.; San Diego, CA: Academic Press)
Mathis, J. S., Rumpl, W., & Nordsieck, K. H. 1977, ApJ, 217, 425
Montalto, M. 2010, A&A, 521, A60
Ordal, M. A. 1988, ApOpt, 27, 1203
Perez-Becker, D., & Chiang, E. 2013, MNRAS, 433, 2294
Perez-Becker, D., & Showman, A. P. 2013, ApJ, 776, 134
Puget, P., Stadler, E., Doyon, R., et al. 2004, Proc. SPIE, 5492, 978
Rappaport, S., Barclay, T., DeVore, J., et al. 2014, ApJ, 784, 40
Rappaport, S., Levine, A., Chiang, E., et al. 2012, ApJ, 752, 1
Rayleigh, L. 1871, PMag, 41, 274
van de Hulst, H. C. 1981, Light Scattering by Small Particles (New York: Dover)
van Werkhoven, T. I. M., Brogi, M., Snellen, I. A. G., & Keller, C. U. 2014, A&A, 561, A3
Vogt, S. S., Allen, S. L., Bigelow, B. C., et al. 1994, Proc. SPIE, 2198, 362
Winn, J. N., Holman, M. J., Torres, G., et al. 2008, ApJ, 683, 1076
Wizinowich, P., Acton, D. S., Shelton, C., et al. 2000, PASP, 112, 315